

Topological Superconductivity by Engineering Noncollinear Magnetism in Magnet/Superconductor Heterostructures: A Realistic Prescription for 2D Kitaev Model

Pritam Chatterjee ^{1,2,*}, Sayan Banik ^{3,*}, Sandip Bera ³, Arnob Kumar Ghosh ^{1,2}, Saurabh Pradhan ⁴, Arijit Saha ^{1,2,†} and Ashis K. Nandy ^{3,‡}

¹*Institute of Physics, Sachivalaya Marg, Bhubaneswar-751005, India*

²*Homi Bhabha National Institute, Training School Complex, Anushakti Nagar, Mumbai 400094, India*

³*School of Physical Sciences, National Institute of Science Education and Research, An OCC of Homi Bhabha National Institute, Jatni 752050, India*

⁴*Lehrstuhl für Theoretische Physik II, Technische Universität Dortmund Otto-Hahn-Str. 4, 44221 Dortmund, Germany*

We report on a realistic and rather general scheme where noncollinear magnetic textures proximitized with the most common s -wave superconductor can appear as the alternative to p -wave superconductor—the prime proposal to realize two-dimensional (2D) Kitaev model for topological superconductors (TSCs) hosting Majorana flat edge mode (MFEM). A general minimal Hamiltonian suitable for magnet/superconductor heterostructures reveals robust MFEM within the gap of Shiba bands due to the emergence of an effective “ $p_x + p_y$ ”-type p -wave pairing, spatially localized at the edges of a 2D magnetic domain of spin-spiral. We finally verify this concept by considering Mn (Cr) monolayer grown on a s -wave superconducting substrate, Nb(110) under strain (Nb(001)). In both 2D cases, the antiferromagnetic spin-spiral solutions exhibit robust MFEM at certain domain edges that is beyond the scope of the trivial extension of 1D spin-chain model in 2D. This approach, particularly when the MFEM appears in the TSC phase for such heterostructure materials, offers a perspective to extend the realm of the TSC in 2D.

Introduction.— A strong quest for topological superconductors (TSCs) hosting Majorana zero-modes (MZMs) [1–9] has been accumulating an immense interest based on magnetic adatoms fabricated on top of an s -wave superconductor (SC) substrate [10–32]. These magnetic atoms in the presence of superconductivity lead to the formation of Yu-Shiba-Rusinov (YSR)/Shiba bands [10, 11, 33] inside the superconducting gap. The mini gap created within such bands plays a pivotal role in exhibiting topological MZMs [10, 11, 34–39] through phase transitions, akin to the one-dimensional Kitaev model (1D-KM) [1, 4]. Generally, the corresponding features like the Shiba states and/or the MZMs are experimentally detected [40–46] in an 1D spin-chain mimicking a trail of magnetic impurities when grown on an s -wave SC. It is essential to highlight that a transition from a 1D finite ferromagnetic (FM) spin chain model with Rashba SOC to its 2D counterpart (FM finite domain) reveals fresh and unique phenomena: the TSC phase in 1D is manifested through the emergence of MZMs [47, 48] while a generalized “ $p_x + ip_y$ ”-type pairing governing 2D TSC phase brings higher Chern numbers and dispersive chiral Majorana edge modes [49, 50]. Preserving all essential terms in those models, this dimensional extension in the problem introduces unique and distinct physics beyond the scope of its 1D counterpart. Therefore, moving to 2D-KM, the prime proposal turns out to be the p -wave SCs and thus, there has been a growing consensus on realizing p -wave SCs in materials despite its rarity so far.

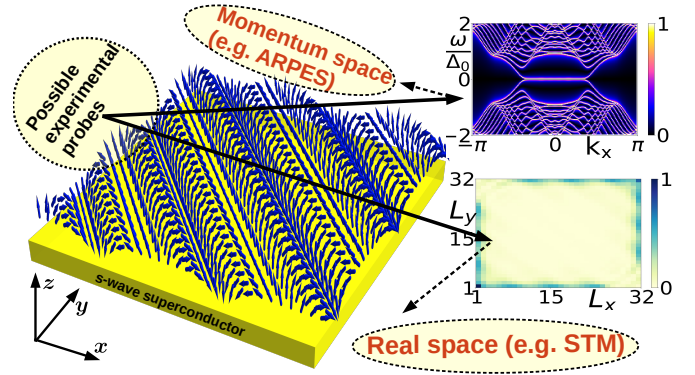


FIG. 1. The schematic setup of our model, a 2D square lattice with SS state placed on the surface of an s -wave SC. Two possible experimental schemes to probe MFEM: the momentum space probe (*e.g.*, ARPES), measures the spectral function as a signature of the MFEM and the real space probe (*e.g.*, STM), measures the spatial distribution of the MFEM at edges, see the corresponding right images.

A distinct signature of such TSCs is non-dispersive Majorana flat edge modes (MFEMs) localized at edges of a 2D domain, can be probed experimentally using scanning tunnelling microscopy (STM) and angle resolved photo emission spectroscopy (ARPES) .

Recently, theoretical proposals for the 2D-KM with topological gapless phase hosting MFEMs has been put forward by employing ($p_x + p_y$)-SCs [51, 52]. A few alternative schemes using inhomogeneous magnetic fields, various magnetic orders *etc* were also explored to generate different p -wave pairing [53–55]. Although a formal connection involving both model and real materials, manifesting similar behavior has never been proposed in this context. Hence, we can address the following in-

* These authors contributed equally to this work

† arijit@iopb.res.in

‡ aknandy@niser.ac.in

triguing questions that have not been answered so far to the best of our knowledge: (a) Can we architect and identify magnetic heterostructures where the spin-spiral (SS) solution in the presence of s -wave SC exhibits features of 2D-KM? (b) Is it possible to derive an effective continuum model consisting of an induced effective spin-orbit coupling (SOC) and Zeeman field to describe such system? (c) Finally and the most importantly, can we identify prototype systems where the SS ground state exhibits gapless TSC phase hosting MFEM within a lattice model? By stabilizing the SS state in 2D films comprising of 3d transition metal (TM) monolayer and s -wave SC substrate may offer the most promising platform for stabilizing the TSC phase in experiments.

In this letter, we first deal with the SS textures in 2D, mimicking spatially varying magnetic impurities proximitized with a s -wave SC. An effective $(p_x + p_y)$ -SC pairing is identified for the SS propagating along $[110]$ direction in a square domain, manifesting gapless TSC phase. Note, the signature of the TSC phase *i.e.*, the nondispersive MFEMs cannot be obtained by straightforward generalization of 1D system [11]. The interplay between the SS state and s -wave SC in our minimal model leads to the emergence of a distinctive “ $p_x + p_y$ ” type SC pairing, supporting the existence of a gapless topological superconducting phase in 2D. At the end, the designed TM/SC heterostructures must reveal SS ground state. We design potential material candidates: one monolayer of Mn and Cr on Nb(110) and Nb(001) SC substrates, respectively. Experimentally observed in-gap YSR band in Mn/Nb(110) [56] is well reproduced within our minimal model, owing to the proximity induced SC in the antiferromagnetic (AFM) state. By looking other aspects of 2D noncollinear magnets [57–59], we apply uniform biaxial strain for engineering AFM-SS state as the ground state in Mn/Nb(110). The AFM-SS within a lattice model reveals TSC phase hosting MFEM. The TSC phase is further observed in another example, unstrained Cr/Nb(001). Hence, such real materials platform adds significant merit to the problem we are dealing with.

Formulation of 2D Kitaev continuum model.— Within a continuum model, we first propose a general route to design 2D gapless TSC phase via engineering SS textures, when proximitized with an s -wave SC. The 2D model Hamiltonian for locally varying magnetic impurities reads in the Nambu spinor form, $\Psi(\mathbf{r}) = (c_{\mathbf{r},\uparrow}, c_{\mathbf{r},\downarrow}, c_{\mathbf{r},\downarrow}^\dagger, -c_{\mathbf{r},\uparrow}^\dagger)^\top$ as $\mathcal{H}_{2D} = \int d\mathbf{r} \Psi^\dagger(\mathbf{r}) H \Psi(\mathbf{r})$, where $c_{\mathbf{r},\uparrow(\downarrow)}$ represents the quasiparticle annihilation operator for the up (down) spin at $\mathbf{r}=(x, y)$. The first quantized form of this Hamiltonian reads,

$$H = -\frac{1}{2} \nabla^2 \tau_z - J \mathbf{S}(\mathbf{r}) \cdot \boldsymbol{\sigma} + \Delta_0 \tau_x - \mu \tau_z. \quad (1)$$

For simplicity, we consider $\hbar=1$ and $m=1$. The Pauli matrices σ and τ acts on the spin and particle-hole subspace, respectively. J , Δ_0 and μ denote the local exchange-interaction strength between the magnetic impurity spin and electrons in the SC, the s -wave order parameter and

the chemical potential, respectively. We assume the impurity spins to be classical and confined in the xy -plane with magnitude $|\mathbf{S}|=1$. Therefore, spin vector $\mathbf{S}(\mathbf{r})$ can be locally described as $\mathbf{S}(\mathbf{r})=|\mathbf{S}|(\cos[\phi(\mathbf{r})], \sin[\phi(\mathbf{r})], 0)$ with $\phi(\mathbf{r})$, the angle between two adjacent spins. By a unitary transformation $U=e^{-\frac{i}{2}\phi(\mathbf{r})\sigma_z}$, an effective low-energy Hamiltonian $\tilde{H}=U^\dagger H U$ in 2D becomes,

$$\tilde{H} = -\frac{1}{2} \sum_{r_i=x,y} \left[\nabla_{r_i}^2 - \left(\frac{\partial \phi}{\partial r_i} \right)^2 - \left(i \frac{\partial \phi}{\partial r_i} \nabla_{r_i} + i \nabla_{r_i} \frac{\partial \phi}{\partial r_i} \right) \sigma_z \right] \tau_z - J \sigma_x + \Delta_0 \tau_x - \mu \tau_z. \quad (2)$$

Note, the similar mapping was reported for 1D spin chain model in case of Majorana bound state solution [60].

Henceforth, we assume that the SS is propagating along the diagonal of a square domain as depicted in Fig. 1, effectively along $[110]$ direction. The angle, $\phi(\mathbf{r})=\mathbf{g} \cdot \mathbf{r}=(g_x x + g_y y)$, defines the angle between two adjacent spins along the SS propagation direction where g_x and g_y values control the SS period and propagation direction. Generally, for $|g_x| \neq |g_y|$, one finds an asymmetric spin textures where the SS propagates neither $[110]$ nor $[\bar{1}\bar{1}0]$ directions and the Hamiltonian \tilde{H} in Eq. (2) can be rewritten in the momentum space as

$$\tilde{H}(\mathbf{k}) = \xi_{\mathbf{k},\mathbf{g}} \tau_z + \frac{1}{2} \mathbf{g} \cdot \mathbf{k} \sigma_z \tau_z + J \sigma_x + \Delta_0 \tau_x, \quad (3)$$

where, $\xi_{\mathbf{k},\mathbf{g}} = \frac{1}{2} (\mathbf{k}^2 + \mathbf{g}^2) - \mu$. The second term represents an effective SOC, resulting from the spin texture in our model. Although, the nature of such SOC is quite nontrivial as it originates from the spin texture, it can interestingly show a gapless TSC phase in the presence of Zeeman like field of strength J along the x -direction. We obtain the spectrum for the Hamiltonian $\tilde{H}(\mathbf{k})$ Eq. (3) as, $E_{r,s}(\mathbf{k}, \mathbf{g}) = r \sqrt{J^2 + \Delta_0^2 + \xi_{\mathbf{k},\mathbf{g}}^2 + \frac{1}{4} \mathbf{k} \cdot \mathbf{g} + s F(\mathbf{k}, \mathbf{g})}$; where, $r, s = \pm$ and $F(\mathbf{k}, \mathbf{g}) = \sqrt{[(\mathbf{k} \cdot \mathbf{g})^2 + 4J^2]^2 \xi_{\mathbf{k},\mathbf{g}}^2 + 4J^2 \Delta_0^2}$. Following the gap closing condition corresponding to the two lowest energy bands, the critical value of J becomes $J_c(\mathbf{g}) = \sqrt{\Delta_0^2 + (\mu - \mathbf{g}^2/2)^2}$. The SS period now can be manifested like $T = \pi/|\mathbf{g}| = \pi/\sqrt{g_x^2 + g_y^2}$ [60]. Hence, in case of $|g_x|=|g_y|=g$, the period turns out to be $T = \pi/\sqrt{2}g$. Naively, the SS solution is governed by the RKKY-type (Ruderman-Kittel-Kasuya-Yosida) exchange frustration and if the period of SS is set by the Fermi momentum \mathbf{k}_F , then $T = \pi/|\mathbf{g}| = \pi/|\mathbf{k}_F|$ [12–14, 60]. In such case, the topological transition occurs at $J_c = \Delta_0$ so that $\mu = |\mathbf{k}_F|^2/2$. However, in real TM/SC systems, the SS solution is the outcome of a complex interplay of material dependent parameters: the exchange coupling constants, \mathcal{J}_{ij} 's; the Dzyaloshinskii-Moriya Interactions (DMIs), \mathbf{D}_{ij} 's; and the uniaxial magneto crystalline anisotropy, \mathcal{K} .

The band structure of this system has been analyzed using the lattice version of the Hamiltonian $\tilde{H}(\mathbf{k})$ defined as $\tilde{H}_L(\mathbf{k})$, see Eq. (S1) in the supplementary materials (SM), Section S1 [61]. We depict the bulk band

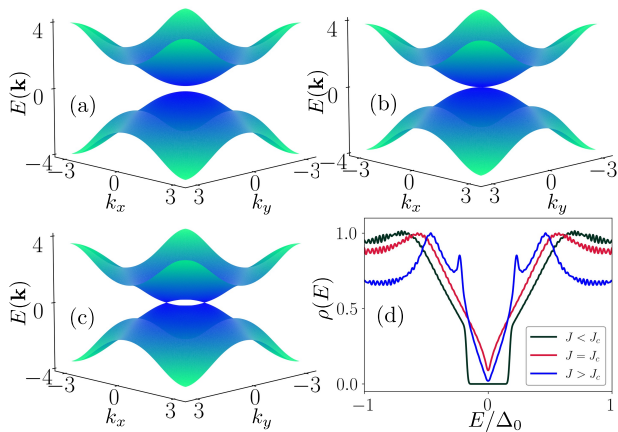


FIG. 2. The bulk band structures of the Hamiltonian $\tilde{H}_L(\mathbf{k})$ in the k_x - k_y plane is depicted for (a) the trivially gapped SC phase, $J < J_c (=1.6\Delta_0)$, (b) the gap closing transition point, $J = J_c (=1.77\Delta_0)$, and (c) the gapless TSC phase hosting MFEM, $J > J_c (=2.0\Delta_0)$. (d) TDOS, $\rho(E)$, is shown as a function of E/Δ_0 for the above mentioned J values in the parenthesis. All remaining parameters take values: $g_x=g_y=\pi/2$, $\mu=\Delta_0=t$.

structure of $\tilde{H}_L(\mathbf{k})$ and the corresponding total density of states (TDOS) $\rho(E)$ in Fig. 2. The topological phase transition occurs between a normal SC phase with a trivial gap, Fig. 2(a) for $J < J_c$ to the gapless TSC phase, Fig. 2(c) for $J > J_c$ via a gap closing phase, Fig. 2(b) at $J = J_c = 1.77\Delta_0$. The topological characterization via appropriate topological invariant (ν) is provided in the SM, Section S1 [61]. The invariant ν changes from 0 to 1 and hence, the system undergoes a transition from a trivial gapped state ($J < J_c$) to a non-trivial ($J > J_c$) TSC phase. This gapless phase displays graphene like semimetallic behavior [62, 63] where $\rho(E)$ corresponding to the gapless TSC phase ($J > J_c$) varies almost linearly with E , see Fig. 2(d). The band structure illustrated in Fig. 2(c) resembles that of the 2D-KM in the TSC phase, reported recently in Refs. [51, 52]. There, the idea of 2D-KM hosting MFEM has been analytically formulated considering $(p_x + p_y)$ -SCs. Indeed, we derive an effective “ $p_x + p_y$ ” SC pairing [based on Eq. (3)] as a result of a domain of SS states propagating along the [110] direction when it is proximitized with an s -wave SC, see details in Section S6 in the SM [61]. Moreover, the inclusion of Rashba SOC in our model and the extension to multi-orbitals [64, 65] (see Section S7 in the SM [61]) do not significantly affect the presence and characteristics of MFEMs. These results seemingly ensure that the crucial prerequisite for the TSC phase is the noncollinear SS state stabilized in TM/SC systems.

In a slab geometry, we then calculate the spectral function, $\mathcal{A}(k_x, \omega)$ [66]. Fig. 3 shows the behavior of $\mathcal{A}(k_x, \omega)$ as a function of energy, ω/Δ_0 . Indeed, the MFEM signature is found clearly in the gapless TSC phase in Fig. 3(c). Fig. 3(a) shows a trivial gap, *i.e.*, without any signature of MFEM and in Fig. 3(b) for $J = J_c$, the edge modes in $\mathcal{A}(k_x, \omega)$ plot are still infinitesimally gaped. Experimen-

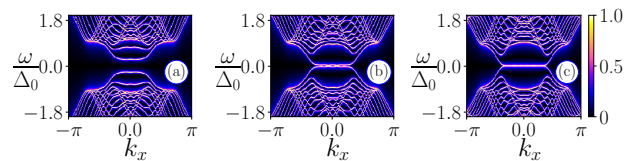


FIG. 3. Panels (a)-(c), the density plots of $\mathcal{A}(k_x, \omega)$ in the k_x - ω plane. A signature of the MFEM is seen in panel (c) for $J > J_c (=2.0\Delta_0)$ where the bulk is a gapless TSC. We choose the same set of respective parameters as mentioned in Fig. 2.

tally, one can probe these signatures of TSC phase using ARPES measurements but such a small gap close to the transition point will be impossible to resolve.

2D Kitaev lattice model for TM/SC heterostructure.—

Focusing on realistic materials framework, we rationalize the above described phenomena using their magnetic ground states. We, therefore, design two prototype TM/SC heterostructures based on 3d-TM monolayer grown on s -wave SC substrates: Mn/Nb(110) and Cr/Nb(001). The Mn/Nb(110) example with its relaxed film geometry constructed with the optimized lattice constant of bulk Nb [67] indeed show a $c(2 \times 2)$ AFM order as the ground state (for detail results, see SM, Section S3(A) [61]), recently reported in experiment also [56]. Surprisingly, we find a transition to an AFM-SS state via a uniform biaxial compressive strain within the range, ~ -1 to -4 %. Considering $a=3.234$ Å and $b=\sqrt{a}=4.574$ Å (strain ~ -2.7 %), Fig. 4(a) illustrates \mathcal{J}_{ij} 's and the absolute values of DMI (\mathcal{D}_{ij}) as a function of distance between Mn atoms and here, \mathcal{K} is positive *i.e.*, out-of-plane. The vector orientations of DMIs in the inset connecting neighboring atoms match the symmetry rules for a system with C_{2v} symmetry [68]. Computational details and more results with varying planar strains on Mn/Nb(110) film are provided in the SM, Section S3(B) [61]. The AFM-SS solution occurs as the stable state even without DMIs, resulting from the strong frustration in \mathcal{J}_{ij} 's connecting Mn moments ($\mathcal{M}_{\text{Mn}} = 3.53 \mu_B$). The significantly weak DMI strengths (< 0.5 meV) are attributed to the weak SOC in light atoms and here, it determines a right-handed cycloidal AFM-SS as the ground state propagating along the [010] direction, see Fig. 4(b).

Here, we elucidate a minimal electronic model Hamiltonian in real space for a 2D lattice,

$$H = - \sum_{\langle i,j \rangle, \alpha} t_{ij} c_{i,\alpha}^\dagger c_{j,\alpha} - \mu \sum_{i,\alpha} c_{i,\alpha}^\dagger c_{j,\alpha} + J \sum_{i,\alpha,\beta} c_{i,\alpha}^\dagger (\hat{\mathbf{s}}_i \cdot \boldsymbol{\sigma})_{\alpha,\beta} c_{i,\beta} + \Delta_0 \sum_i (c_{i,\uparrow}^\dagger c_{i,\downarrow}^\dagger + \text{H.c.}), \quad (4)$$

where, i, j indices run over all the lattice sites, α, β denote the spin, $\langle \rangle$ represents nearest-neighbor hopping only, μ, J, Δ_0 represent the chemical potential, exchange coupling strength, s -wave SC gap, respectively and $c^\dagger(c)$ corresponds to the electron creation (annihilation) operator for the SC. For simplicity, we assume the hopping amplitude $t_{ij}=t_{ji}=-t$ with $t=1$ for the overall energy scale of our system. This minimal Hamiltonian is essentially

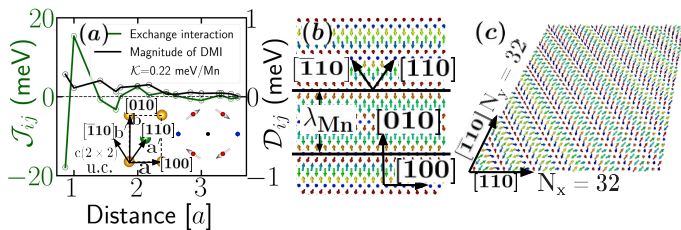


FIG. 4. For Mn/Nb(110) with strain $\sim -2.7\%$, (a) J_{ij} 's and D_{ij} 's are plotted as a function of distance measured in units of lattice constant a . Calculated \mathcal{K} is out-of-plane. Lower left inset shows the $c(2 \times 2)$ -AFM surface unit cell (yellow and green balls represent up and down spins, respectively), possessing C_{2v} symmetry. The lower right inset describes vector-orientations of DMIs. (b) The AFM-SS ground state propagates along the [010] direction. (c) A 32×32 AFM-SS domain where edges are considered along [110] and $[\bar{1}\bar{1}0]$ directions.

constructed to ensure the importance of magnetic textures (alternative to the intrinsic SOC) of TM/SCs in the context of stabilizing TSC phase. All spin textures are actually entered in the third term in Eq. (4), describing a local interaction between the electron's spin (σ) and the moments of Mn or Cr. The unit vector \hat{s}_i denotes $(\sin \theta_i \cos \phi_i, \sin \theta_i \sin \phi_i, \cos \theta_i)$, mimicking locally varying magnetic impurities. One can extract these θ and ϕ from the spin textures generated by the MC simulations for TM/SC systems.

In case of Mn/Nb(110), the $c(2 \times 2)$ AFM phase has been assessed first via numerically solving Eq. (4). Our results indeed describe the experimental findings where the s -wave SC and AFM phases are found to coexist [56], see the SM, Section S3(B) for more details [61]. The in-gap YSR bands ensure the qualitative accuracy of our minimal model in Eq. (4).

A few important results are obtained from the numerical simulations by considering the AFM-SS 2D domain. We construct a domain of size 32×32 (1024 spins) where the AFM-SS is propagating along the diagonal of that domain (as similar in the FM-SS, Fig. 1) with edges along [110] and $[\bar{1}\bar{1}0]$ directions, see Fig. 4(c). Hence, these directions are parallel to the rotated vectors \mathbf{a}' and \mathbf{b}' of the 2D lattice in the inset of Fig. 4(a). The measured θ and ϕ values describe \hat{s} to solve Eq. (4), numerically. Results are summarized in Figs. 5 where, (a) and (b) depict the local density of states (LDOS) for the zero-energy ($E=0$) states using coupling constant, $J=4.5\Delta_0$ and $5.0\Delta_0$, respectively. The zero-energy states populate along the edges of the domain in Fig. 5(a) and hence, the system is in the TSC regime. The MFEM are maximally localized at the two opposite corners of the system and disperse gradually along the edges. Moreover, the signature of the MFEM is more evident from the non-dispersive states at $E_n=0$ in the eigenvalue spectrum plotted as a function of the state index n in the inset of Fig. 5(a). The semimetallic behavior of the bulk YSR band at $J=4.5\Delta_0$ presented in the SM, Section S5 [61] for the TSC regime qualitatively matches with the continuum results presented in Fig. 2(d). The inset of Fig. 5(b) shows a trivial phase by

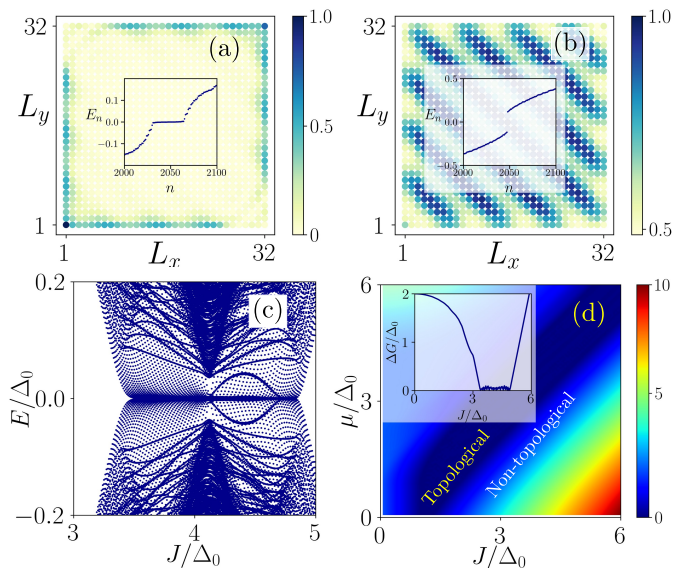


FIG. 5. The normalized LDOS for $E=0$ eigenstate, computed within a spin lattice model of size 32×32 spins (L_x - L_y square plane). Here, 2D lattice points are defined in unit of, \mathbf{a}' and \mathbf{b}' , as shown in the inset of Fig. 4(a). For Mn/Nb(110) with AFM-SS state, (a) we identify the TSC phase for $J=4.5\Delta_0$. The LDOS is predominantly localized at the domain edges denoting MFEMs. (b) In the trivial phase for $J=5.0\Delta_0$, LDOS is delocalized over the entire domain. Insets in (a) and (b) show a zero-energy flat mode and a trivial gap in the eigenvalue E_n vs. state n plots, respectively. (c) Energy eigenvalues E of H is shown as a function of J using OBC. (d) The bulk-gap ΔG profile is shown in the J - μ plane employing PBC, indicating the TSC phase (dark blue regime). The inset is showing ΔG vs. J plot for a fixed μ ($=4.0\Delta_0$ and $\Delta_0=t$).

opening a gap in the eigenvalue spectrum around $E_n=0$.

Seemingly, it appears that the coupling constant J (rather, J/Δ_0) plays a major role in the phase transition between trivial SC and TSC phases. Particularly, J value is often very challenging to determine for such materials. Therefore, in Fig. 5(c), we depict the eigenvalue spectrum E/Δ_0 as a function of J/Δ_0 by employing open boundary condition (OBC). The MFEM appears at zero-energy between $J=3.5\Delta_0$ and $J=4.7\Delta_0$, indicating the TSC regime. We thereafter identify the parameter regime where the MFEM appears via calculating the bulk-gap, $\Delta G=|E_2-E_1|$, within periodic boundary condition (PBC). Here, E_1 (E_2) represents the two low energy bands. We depict $\Delta G/\Delta_0$ in the J/Δ_0 - μ/Δ_0 plane in Fig. 5(d). The gapless TSC regime harboring MFEM is highlighted by the dark blue strip ($\Delta G \simeq 0$), while the regime outside ($\Delta G > 0$) represents gapped trivial superconducting phase. In the inset of Fig. 5(d), we illustrate the bulk-gap ΔG as a function of J for a fixed value of μ , for the transparent visibility of the TSC regime. The bulk-gap ΔG vanishes in the topological regime and MFEM appears at the boundary.

The new example, Cr/Nb(001), shows left-handed cycloidal AFM-SS as the ground state without strain, propagating along both [100] and [010] degenerate directions. The degeneracy is owing to the symmetry rules followed

by the DMI vectors in the C_{4v} symmetric film [68]. We solve Eq. (4) again for the square domains and all results are presented in the SM, Section S4 [61].

Summary and outlook.— In conclusion, by employing a continuum model, we demonstrate a route to generate a gapless TSC phase hosting MFEMs by engineering non-collinear SS state proximitized with an s -wave superconductor. This underlying scheme is later extended within a minimal lattice model which provides a unique way to unveil the TSC phase in prototype real TM/SC (s -wave) materials: Mn/Nb(110) under strain and Cr/Nb(001). Even though, the SOC strength in Nb is expected to be very small, the AFM-SS can be stabilized from the exchange frustration, particularly in the Mn/Nb(110) sample and thereby, an effective SOC and Zeeman field terms due to the spin textures manifest the Hamiltonian obtained in Eq. (3). The immobile MFEMs can be thought of edge channels to carry edge vortices in Josephson junction geometries—offering a possibility for non-Abelian “braiding” operations [69, 70]. Note that, similar idea

has been demonstrated in the context of braiding mobile vortices via the chiral dispersive edge channels in 2D [71]. Importantly, the investigation of this “braiding” protocols for MFEMs is an intriguing and important direction for future studies. Indeed, our realistic model Hamiltonian unveils excellent examples where the strain driven modulation of the noncollinear magnetic phases can offer unprecedented control over various types of TSC phases including 2D-KM, higher-order topological superconductors [72], AFM-SC spintronics [73] in near future.

Acknowledgments.— The first-principle calculations in this letter is supported by the Swedish National Infrastructure for Computing (SNIC) facility and for that, S.B. and A. K. N. sincerely thank Prof. P. M. Oppeneer. P.C., S.B, A.K.G., A.S. and A. K. N. acknowledge the support from Department of Atomic Energy (DAE), Govt. of India. S B. and A.K.N. acknowledge the KALINGA HPC facility at NISER, Bhubaneswar and P.C., A.K.G. and A.S. acknowledge the SAMKHYA: HPC Facility provided at IOP, Bhubaneswar, for numerical computations.








-
- [1] A Yu Kitaev, “Unpaired majorana fermions in quantum wires,” *Physics-Uspekhi* **44**, 131 (2001).
- [2] D. A. Ivanov, “Non-abelian statistics of half-quantum vortices in p -wave superconductors,” *Phys. Rev. Lett.* **86**, 268–271 (2001).
- [3] Chetan Nayak, Steven H. Simon, Ady Stern, Michael Freedman, and Sankar Das Sarma, “Non-abelian anyons and topological quantum computation,” *Rev. Mod. Phys.* **80**, 1083–1159 (2008).
- [4] Alexei Kitaev, “Periodic table for topological insulators and superconductors,” *AIP Conference Proceedings* **1134**, 22–30 (2009).
- [5] Xiao-Liang Qi and Shou-Cheng Zhang, “Topological insulators and superconductors,” *Rev. Mod. Phys.* **83**, 1057 (2011).
- [6] Jason Alicea, “New directions in the pursuit of majorana fermions in solid state systems,” *Reports on Progress in Physics* **75**, 076501 (2012).
- [7] Martin Leijnse and Karsten Flensberg, “Introduction to topological superconductivity and majorana fermions,” *Semiconductor Science and Technology* **27**, 124003 (2012).
- [8] CWJ Beenakker, “Search for majorana fermions in superconductors,” *Annu. Rev. Condens. Matter Phys.* **4**, 113–136 (2013).
- [9] R. Aguado, “Majorana quasiparticles in condensed matter,” *Riv. Nuovo Cimento* **40**, 523 (2017).
- [10] Falko Pientka, Leonid I. Glazman, and Felix von Oppen, “Topological superconducting phase in helical shiba chains,” *Phys. Rev. B* **88**, 155420 (2013).
- [11] S. Nadj-Perge, I. K. Drozdov, B. A. Bernevig, and Ali Yazdani, “Proposal for realizing majorana fermions in chains of magnetic atoms on a superconductor,” *Phys. Rev. B* **88**, 020407 (2013).
- [12] Jelena Klinovaja, Peter Stano, Ali Yazdani, and Daniel Loss, “Topological superconductivity and majorana fermions in rkky systems,” *Phys. Rev. Lett.* **111**, 186805 (2013).
- [13] Bernd Braunecker and Pascal Simon, “Interplay between classical magnetic moments and superconductivity in quantum one-dimensional conductors: Toward a self-sustained topological majorana phase,” *Phys. Rev. Lett.* **111**, 147202 (2013).
- [14] M. M. Vazifeh and M. Franz, “Self-organized topological state with majorana fermions,” *Phys. Rev. Lett.* **111**, 206802 (2013).
- [15] Jay D. Sau and Eugene Demler, “Bound states at impurities as a probe of topological superconductivity in nanowires,” *Phys. Rev. B* **88**, 205402 (2013).
- [16] Falko Pientka, Leonid I. Glazman, and Felix von Oppen, “Unconventional topological phase transitions in helical shiba chains,” *Phys. Rev. B* **89**, 180505 (2014).
- [17] Kim Pöyhönen, Alex Westström, Joel Röntynen, and Teemu Ojanen, “Majorana states in helical shiba chains and ladders,” *Phys. Rev. B* **89**, 115109 (2014).
- [18] I. Reis, D. J. J. Marchand, and M. Franz, “Self-organized topological state in a magnetic chain on the surface of a superconductor,” *Phys. Rev. B* **90**, 085124 (2014).
- [19] Wenjian Hu, Richard T. Scalettar, and Rajiv R. P. Singh, “Interplay of magnetic order, pairing, and phase separation in a one-dimensional spin-fermion model,” *Phys. Rev. B* **92**, 115133 (2015).
- [20] Hoi-Yin Hui, P. M. R. Brydon, Jay D. Sau, S. Tewari, and S. Das Sarma, “Majorana fermions in ferromagnetic chains on the surface of bulk spin-orbit coupled s -wave superconductors,” *Scientific Reports* **5**, 8880 (2015).
- [21] Silas Hoffman, Jelena Klinovaja, and Daniel Loss, “Topological phases of inhomogeneous superconductivity,” *Phys. Rev. B* **93**, 165418 (2016).
- [22] Morten H. Christensen, Michael Schecter, Karsten Flensberg, Brian M. Andersen, and Jens Paaske, “Spiral magnetic order and topological superconductivity in a chain of magnetic adatoms on a two-dimensional superconductor,” *Phys. Rev. B* **94**, 144509 (2016).
- [23] Girish Sharma and Sumanta Tewari, “Yu-shiba-rusinov states and topological superconductivity in ising paired

- superconductors,” *Phys. Rev. B* **94**, 094515 (2016).
- [24] Gian Marcello Andolina and Pascal Simon, “Topological properties of chains of magnetic impurities on a superconducting substrate: Interplay between the shiba band and ferromagnetic wire limits,” *Phys. Rev. B* **96**, 235411 (2017).
- [25] Andreas Theiler, Kristofer Björnson, and Annica M. Black-Schaffer, “Majorana bound state localization and energy oscillations for magnetic impurity chains on conventional superconductors,” *Phys. Rev. B* **100**, 214504 (2019).
- [26] Doru Sticlet and Cristian Morari, “Topological superconductivity from magnetic impurities on monolayer nbse₂,” *Phys. Rev. B* **100**, 075420 (2019).
- [27] Mahdi Mashkoori and Annica Black-Schaffer, “Majorana bound states in magnetic impurity chains: Effects of d -wave pairing,” *Phys. Rev. B* **99**, 024505 (2019).
- [28] Gerbold C. Mnard, Christophe Brun, Raphael Leriche, Mircea Trif, Francois Debontridder, Dominique Demaille, Dimitri Roditchev, Pascal Simon, and Tristan Cren, “Yu-shiba-rusinov bound states versus topological edge states in Pb/Si(111),” *The European Physical Journal Special Topics* **227**, 2303–2313 (2019).
- [29] Mahdi Mashkoori, Saurabh Pradhan, Kristofer Björnson, Jonas Fransson, and Annica M. Black-Schaffer, “Identification of topological superconductivity in magnetic impurity systems using bulk spin polarization,” *Phys. Rev. B* **102**, 104501 (2020).
- [30] Raphael L. R. C. Teixeira, Dushko Kuzmanovski, Annica M. Black-Schaffer, and Luis G. G. V. Dias da Silva, “Enhanced majorana bound states in magnetic chains on superconducting topological insulator edges,” *Phys. Rev. B* **102**, 165312 (2020).
- [31] Stefan Rex, Igor V. Gornyi, and Alexander D. Mirlin, “Majorana modes in emergent-wire phases of helical and cycloidal magnet-superconductor hybrids,” *Phys. Rev. B* **102**, 224501 (2020).
- [32] Vivien Perrin, Marcello Civelli, and Pascal Simon, “Identifying majorana bound states by tunneling shot-noise tomography,” *Phys. Rev. B* **104**, L121406 (2021).
- [33] Hiroyuki Shiba, “Classical Spins in Superconductors,” *Progress of Theoretical Physics* **40**, 435–451 (1968).
- [34] V Kaladzhyan, C Bena, and P Simon, “Asymptotic behavior of impurity-induced bound states in low-dimensional topological superconductors,” *Journal of Physics: Condensed Matter* **28**, 485701 (2016).
- [35] Ning Dai, Kai Li, Yan-Bin Yang, and Yong Xu, “Topological quantum phase transitions in metallic shiba lattices,” *Phys. Rev. B* **106**, 115409 (2022).
- [36] Jon Ortuzar, Stefano Trivini, Miguel Alvarado, Mikel Rouco, Javier Zaldivar, Alfredo Levy Yeyati, Jose Ignacio Pascual, and F. Sebastian Bergeret, “Yu-shiba-rusinov states in two-dimensional superconductors with arbitrary fermi contours,” *Phys. Rev. B* **105**, 245403 (2022).
- [37] Areg Ghazaryan, Ammar Kirmani, Rafael M. Fernandes, and Pouyan Ghaemi, “Anomalous shiba states in topological iron-based superconductors,” *Phys. Rev. B* **106**, L201107 (2022).
- [38] Harald Schmid, Jacob F. Steiner, Katharina J. Franke, and Felix von Oppen, “Quantum yu-shiba-rusinov dimers,” *Phys. Rev. B* **105**, 235406 (2022).
- [39] Pritam Chatterjee, Saurabh Pradhan, Ashis K. Nandy, and Arijit Saha, “Tailoring the phase transition from topological superconductor to trivial superconductor induced by magnetic textures of a spin chain on a p -wave superconductor,” *Phys. Rev. B* **107**, 085423 (2023).
- [40] Ali Yazdani, B. A. Jones, C. P. Lutz, M. F. Crommie, and D. M. Eigler, “Probing the local effects of magnetic impurities on superconductivity,” *Science* **275**, 1767–1770 (1997).
- [41] Ali Yazdani, C. M. Howald, C. P. Lutz, A. Kapitulnik, and D. M. Eigler, “Impurity-induced bound excitations on the surface of $Bi_2Sr_2CaCu_2O_8$,” *Phys. Rev. Lett.* **83**, 176–179 (1999).
- [42] Ali Yazdani, “Visualizing majorana fermions in a chain of magnetic atoms on a superconductor,” *Physica Scripta* **2015**, 014012 (2015).
- [43] Lucas Schneider, Philip Beck, Thore Posske, Daniel Crawford, Eric Mascot, Stephan Rachel, Roland Wiesendanger, and Jens Wiebe, “Topological shiba bands in artificial spin chains on superconductors,” *Nature Physics* **17**, 943–948 (2021).
- [44] Philip Beck, Lucas Schneider, Levente Rózsa, Krisztián Palotás, András Lászlóffy, László Szunyogh, Jens Wiebe, and Roland Wiesendanger, “Spin-orbit coupling induced splitting of yu-shiba-rusinov states in antiferromagnetic dimers,” *Nature Communications* **12**, 2040 (2021).
- [45] Dongfei Wang, Jens Wiebe, Ruidan Zhong, Genda Gu, and Roland Wiesendanger, “Spin-polarized yu-shiba-rusinov states in an iron-based superconductor,” *Phys. Rev. Lett.* **126**, 076802 (2021).
- [46] Lucas Schneider, Philip Beck, Jannis Neuhaus-Steinmetz, Levente Rózsa, Thore Posske, Jens Wiebe, and Roland Wiesendanger, “Precursors of majorana modes and their length-dependent energy oscillations probed at both ends of atomic shiba chains,” *Nature Nanotechnology* **17**, 384–389 (2022).
- [47] Jian Li, Hua Chen, Ilya K. Drozdov, A. Yazdani, B. Andrei Bernevig, and A. H. MacDonald, “Topological superconductivity induced by ferromagnetic metal chains,” *Phys. Rev. B* **90**, 235433 (2014).
- [48] P. M. R. Brydon, S. Das Sarma, Hoi-Yin Hui, and Jay D. Sau, “Topological yu-shiba-rusinov chain from spin-orbit coupling,” *Phys. Rev. B* **91**, 064505 (2015).
- [49] Joel Rontynen and Teemu Ojanen, “Topological superconductivity and high chern numbers in 2d ferromagnetic shiba lattices,” *Phys. Rev. Lett.* **114**, 236803 (2015).
- [50] Joel Röntynen and Teemu Ojanen, “Chern mosaic: Topology of chiral superconductivity on ferromagnetic adatom lattices,” *Phys. Rev. B* **93**, 094521 (2016).
- [51] P. Wang, S. Lin, G. Zhang, and Z. Song, “Topological gapless phase in kitaev model on square lattice,” *Scientific Reports* **7**, 17179 (2017).
- [52] K. L. Zhang, P. Wang, and Z. Song, “Majorana flat band edge modes of topological gapless phase in 2d kitaev square lattice,” *Scientific Reports* **9**, 4978 (2019).
- [53] N. Sedlmayr, J. M. Aguiar-Hualde, and C. Bena, “Flat majorana bands in two-dimensional lattices with inhomogeneous magnetic fields: Topology and stability,” *Phys. Rev. B* **91**, 115415 (2015).
- [54] Sho Nakosai, Yukio Tanaka, and Naoto Nagaosa, “Two-dimensional p -wave superconducting states with magnetic moments on a conventional s -wave superconductor,” *Phys. Rev. B* **88**, 180503 (2013).
- [55] Wei Chen and Andreas P. Schnyder, “Majorana edge states in superconductor-noncollinear magnet interfaces,” *Phys. Rev. B* **92**, 214502 (2015).
- [56] Roberto Lo Conte, Maciej Bazarnik, Krisztián Palotás,

- Levente Rózsa, László Szunyogh, André Kubetzka, Kirsten von Bergmann, and Roland Wiesendanger, “Coexistence of antiferromagnetism and superconductivity in Mn/Nb(110),” *Phys. Rev. B* **105**, L100406 (2022).
- [57] Ashis Kumar Nandy, Nikolai S. Kiselev, and Stefan Blügel, “Interlayer exchange coupling: A general scheme turning chiral magnets into magnetic multilayers carrying atomic-scale skyrmions,” *Phys. Rev. Lett.* **116**, 177202 (2016).
- [58] Roberto Lo Conte, Ashis K. Nandy, Gong Chen, Andre L. Fernandes Cauduro, Ajanta Maity, Colin Ophus, Zhijie Chen, Alpha T. N’Diaye, Kai Liu, Andreas K. Schmid, and Roland Wiesendanger, “Tuning the properties of zero-field room temperature ferromagnetic skyrmions by interlayer exchange coupling,” *Nano Letters* **20**, 4739–4747 (2020).
- [59] M. Bode, M. Heide, K. von Bergmann, P. Ferriani, S. Heinze, G. Bihlmayer, A. Kubetzka, O. Pietzsch, S. Blügel, and R. Wiesendanger, “Chiral magnetic order at surfaces driven by inversion asymmetry,” *Nature (London)* **447**, 190–193 (2007).
- [60] Richard Hess, Henry F. Legg, Daniel Loss, and Jelena Klinovaja, “Prevalence of trivial zero-energy subgap states in nonuniform helical spin chains on the surface of superconductors,” *Phys. Rev. B* **106**, 104503 (2022).
- [61] See the Supplemental Material (SM), which includes Refs [3, 49, 53, 56, 58, 59, 64, 65, 68–71, 74–99], for the details of the topological characterization, methodology including *ab initio* electronic structure calculations using VASP and KKR-GF and atomistic spin dynamics simulations, results in detail of the strain effect in Mn/Nb(110) example, full details of the new candidate Cr/Nb(001), semimetallic behavior details, derivation of an effective “ $p_x + p_y$ ”-wave pairing and the effect of Rashba SOC in single and multi-orbital scenario.
- [62] A. H. Castro Neto, F. Guinea, N. M. R. Peres, K. S. Novoselov, and A. K. Geim, “The electronic properties of graphene,” *Rev. Mod. Phys.* **81**, 109–162 (2009).
- [63] Katsunori Wakabayashi, Ken ichi Sasaki, Takeshi Nakanishi, and Toshiaki Enoki, “Electronic states of graphene nanoribbons and analytical solutions,” *Science and Technology of Advanced Materials* **11**, 054504 (2010).
- [64] Chaoxing Liu, Taylor L. Hughes, Xiao-Liang Qi, Kang Wang, and Shou-Cheng Zhang, “Quantum spin hall effect in inverted type-II semiconductors,” *Phys. Rev. Lett.* **100**, 236601 (2008).
- [65] Laura Ortiz, Rafael A. Molina, Gloria Platero, and Anders Mathias Lunde, “Generic helical edge states due to rashba spin-orbit coupling in a topological insulator,” *Phys. Rev. B* **93**, 205431 (2016).
- [66] The spectral function $\mathcal{A}(k_x, \omega)$ has been defined through the zero-temperature Green’s function $\hat{G}(k_x, \omega)$ as $\mathcal{A}(k_x, \omega) = -\frac{1}{\pi} \text{Im}[\text{Tr}\{\hat{G}(k_x, \omega)\}]$; where $\hat{G}(k_x, \omega) = [\mathbb{I} - \tilde{H}_L(y, k_x)]^{-1}$.
- [67] Within the generalized gradient approximation (GGA) functional, the optimized lattice constant of bulk body-centered-cubic Nb is found to be $a_{\text{Nb}} = 3.3232 \text{ \AA}$, an excellent agreement with the experimental value of about 3.32 \AA [74]. The value of a_{Nb} is then used to construct the optimized film geometry and also strains are measured with respect to a_{Nb} .
- [68] Tôru Moriya, “Anisotropic superexchange interaction and weak ferromagnetism,” *Phys. Rev.* **120**, 91–98 (1960).
- [69] Jason Alicea, Yuval Oreg, Gil Refael, Felix von Oppen, and Matthew P. A. Fisher, “Non-abelian statistics and topological quantum information processing in 1d wire networks,” *Nature Physics* **7**, 412–417 (2011).
- [70] Geoffrey L. Fatin, Alex Matos-Abiague, Benedikt Scharf, and Igor Žutić, “Wireless majorana bound states: From magnetic tunability to braiding,” *Phys. Rev. Lett.* **117**, 077002 (2016).
- [71] C. W. J. Beenakker, P. Baireuther, Y. Herasymenko, I. Adagideli, Lin Wang, and A. R. Akhmerov, “Deterministic creation and braiding of chiral edge vortices,” *Phys. Rev. Lett.* **122**, 146803 (2019).
- [72] Arnob Kumar Ghosh, Tanay Nag, and Arijit Saha, “Hierarchy of higher-order topological superconductors in three dimensions,” *Phys. Rev. B* **104**, 134508 (2021).
- [73] Leandro Salemi, Marco Berritta, Ashis K. Nandy, and Peter M. Oppeneer, “Orbitally dominated rashba-Edelstein effect in noncentrosymmetric antiferromagnets,” *Nature Communications* **10**, 5381 (2019).
- [74] The Materials Project, “Materials data on Nb by materials project,” [10.17188/1288516](https://doi.org/10.17188/1288516).
- [75] I. Dzyaloshinsky, “A thermodynamic theory of “weak” ferromagnetism of antiferromagnetics,” *Journal of Physics and Chemistry of Solids* **4**, 241–255 (1958).
- [76] Gideon P. Müller, Markus Hoffmann, Constantin Difelkamp, Daniel Schürhoff, Stefanos Mavros, Moritz Sallermann, Nikolai S. Kiselev, Hannes Jónsson, and Stefan Blügel, “Spirit: Multifunctional framework for atomistic spin simulations,” *Phys. Rev. B* **99**, 224414 (2019).
- [77] P.D. Landau and K. Binder, “A guide to monte carlo methods in statistical physics, cambridge university press, cambridge, england,” (2000).
- [78] “P. j. van laarhoven and e. h. aarts, simulated annealing: Theory and applications, (d. reidel, dordrecht, holland, 1987).”.
- [79] Changhoon Heo, Nikolai S. Kiselev, Ashis Kumar Nandy, Stefan Blügel, and Theo Rasing, “Switching of chiral magnetic skyrmions by picosecond magnetic field pulses via transient topological states,” *Scientific Reports* **6**, 27146 (2016).
- [80] Vegard Flovik, Alireza Qaiumzadeh, Ashis K. Nandy, Changhoon Heo, and Theo Rasing, “Generation of single skyrmions by picosecond magnetic field pulses,” *Phys. Rev. B* **96**, 140411 (2017).
- [81] Biao Lian, Xiao-Qi Sun, Abolhassan Vaezi, Xiao-Liang Qi, and Shou-Cheng Zhang, “Topological quantum computation based on chiral majorana fermions,” *Proceedings of the National Academy of Sciences* **115**, 10938–10942 (2018).
- [82] Sandip Bera and Sudhansu S Mandal, “Skyrmions at vanishingly small dzyaloshinskii–moriya interaction or zero magnetic field,” *Journal of Physics: Condensed Matter* **33**, 255801 (2021).
- [83] Sandip Bera and Sudhansu S. Mandal, “Theory of the skyrmion, meron, antiskyrmion, and antimeron in chiral magnets,” *Phys. Rev. Research* **1**, 033109 (2019).
- [84] Masatoshi Sato, Yoshiro Takahashi, and Satoshi Fujimoto, “Non-abelian topological order in *s*-wave superfluids of ultracold fermionic atoms,” *Phys. Rev. Lett.* **103**, 020401 (2009).
- [85] Masatoshi Sato, Yoshiro Takahashi, and Satoshi Fujimoto, “Non-abelian topological orders and majorana fermions in spin-singlet superconductors,” *Phys. Rev. B*

- 82**, 134521 (2010).
- [86] Jürgen Hafner, “Ab-initio simulations of materials using vasp: Density-functional theory and beyond,” *Journal of computational chemistry* **29**, 2044–2078 (2008).
 - [87] Georg Kresse and Jürgen Furthmüller, “Efficiency of ab-initio total energy calculations for metals and semiconductors using a plane-wave basis set,” *Computational materials science* **6**, 15–50 (1996).
 - [88] G. Kresse and J. Furthmüller, “Efficient iterative schemes for ab initio total-energy calculations using a plane-wave basis set,” *Phys. Rev. B* **54**, 11169–11186 (1996).
 - [89] John P. Perdew, Kieron Burke, and Matthias Ernzerhof, “Generalized gradient approximation made simple,” *Phys. Rev. Lett.* **77**, 3865–3868 (1996).
 - [90] G. Kresse and D. Joubert, “From ultrasoft pseudopotentials to the projector augmented-wave method,” *Phys. Rev. B* **59**, 1758–1775 (1999).
 - [91] P. E. Blöchl, “Projector augmented-wave method,” *Phys. Rev. B* **50**, 17953–17979 (1994).
 - [92] D. S. G. Bauer, “Development of a relativistic full-potential first-principles multiple scattering green function method applied to complex magnetic textures of nano structures at surfaces.” Ph.D. Thesis, RWTH Aachen (2013).
 - [93] A.I. Liechtenstein, M.I. Katsnelson, V.P. Antropov, and V.A. Gubanov, “Local spin density functional approach to the theory of exchange interactions in ferromagnetic metals and alloys,” *Journal of Magnetism and Magnetic Materials* **67**, 65–74 (1987).
 - [94] J. Zabludil, R. Hammerling, L. Szunyogh, and Weinberger P., “Electron scattering in solid matter: A theoretical and computational treatise (springer, 2005),”.
 - [95] Seymour H Vosko, Leslie Wilk, and Marwan Nusair, “Accurate spin-dependent electron liquid correlation energies for local spin density calculations: a critical analysis,” *Canadian Journal of physics* **58**, 1200–1211 (1980).
 - [96] L. Udvardi, L. Szunyogh, K. Palotás, and P. Weinberger, “First-principles relativistic study of spin waves in thin magnetic films,” *Phys. Rev. B* **68**, 104436 (2003).
 - [97] H. Ebert and S. Mankovsky, “Anisotropic exchange coupling in diluted magnetic semiconductors: Ab initio spin-density functional theory,” *Phys. Rev. B* **79**, 045209 (2009).
 - [98] A. Fert and Peter M. Levy, “Role of anisotropic exchange interactions in determining the properties of spin-glasses,” *Phys. Rev. Lett.* **44**, 1538–1541 (1980).
 - [99] P. Ferriani, K. von Bergmann, E. Y. Vedmedenko, S. Heinze, M. Bode, M. Heide, G. Bihlmayer, S. Blügel, and R. Wiesendanger, “Atomic-scale spin spiral with a unique rotational sense: Mn monolayer on W(001),” *Phys. Rev. Lett.* **101**, 027201 (2008).

Supplemental material for “Topological Superconductivity by Engineering Noncollinear Magnetism in Magnet/Superconductor Heterostructures: A Realistic Prescription for 2D Kitaev Model”

Pritam Chatterjee ^{1,2}, Sayan Banik ³, Sandip Bera ³, Arnob Kumar Ghosh ^{1,2}, Saurabh Pradhan ⁴, Arijit Saha ^{1,2}, and Ashis K. Nandy ³

¹*Institute of Physics, Sachivalaya Marg, Bhubaneswar-751005, India*

²*Homi Bhabha National Institute, Training School Complex, Anushakti Nagar, Mumbai 400094, India*

³*School of Physical Sciences, National Institute of Science Education and Research, An OCC of Homi Bhabha National Institute, Jatni 752050, India*

⁴*Lehrstuhl für Theoretische Physik II, Technische Universität Dortmund Otto-Hahn-Str. 4, 44221 Dortmund, Germany*

S1. TOPOLOGICAL CHARACTERIZATION

In this section of the supplementary material (SM), we discuss the topological characterization of our model. We begin with the continuum Hamiltonian described in the main text [Eq. (3)]. One can obtain the lattice version of the continuum Hamiltonian by replacing $k_x \rightarrow \sin k_x$, $k_y \rightarrow \sin k_y$, $(1 - k_x^2/2) \rightarrow \cos k_x$, and $(1 - k_y^2/2) \rightarrow \cos k_y$ as

$$\tilde{H}_L(\mathbf{k}) = \xi_{\mathbf{k},\mathbf{g}}\tau_z + \frac{1}{2}(g_x \sin k_x + g_y \sin k_y)\sigma_z\tau_z + J\sigma_x + \Delta_0\tau_x, \quad (\text{S1})$$

where, $\xi_{\mathbf{k},\mathbf{g}} = (2 - \cos k_x - \cos k_y) + \frac{(g_x^2 + g_y^2)}{2} - \mu$. At the high symmetry points $\Gamma_l = [(0,0), (\pi,0), (0,\pi), (\pi,\pi)]$, if we perform the proper basis transformation, then the Hamiltonian in Eq. (S1) can be recast in the block diagonal form as,

$$\tilde{H}_L(\mathbf{k}) = \begin{pmatrix} h(\Gamma_l) & O_{2 \times 2} \\ O_{2 \times 2} & -h(\Gamma_l) \end{pmatrix}. \quad (\text{S2})$$

where,

$$h(\Gamma_l) = \begin{pmatrix} J + \xi_{\mathbf{k},\mathbf{g}}(\Gamma_l) & \Delta_0 \\ \Delta_0 & J - \xi_{\mathbf{k},\mathbf{g}}(\Gamma_l) \end{pmatrix}. \quad (\text{S3})$$

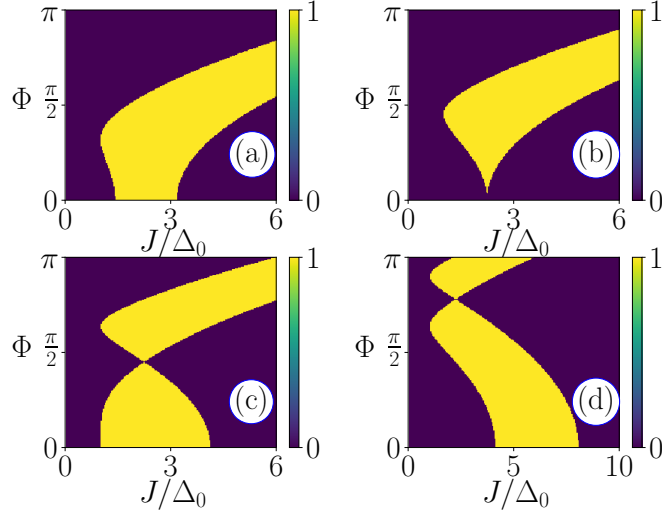


FIG. S1. Topological invariant ν for the symmetric ($g_x = g_y = \Phi$) spin texture is shown. Panels (a), (b), (c), and (d) correspond to the variation of ν in the J - Φ plane for different values of the chemical potential $\mu = \Delta_0, 2.0\Delta_0, 4.0\Delta_0$, and $8.0\Delta_0$, respectively.

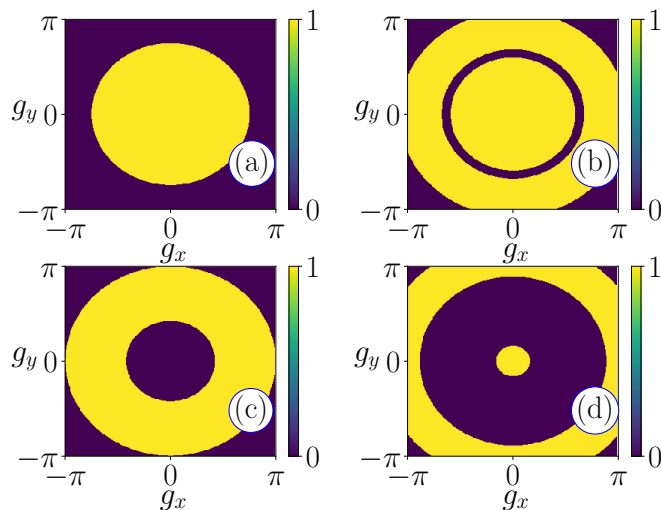


FIG. S2. Topological invariant ν in case of asymmetric spin texture ($g_x \neq g_y$) is depicted. Panels (a), (b), (c), (d) correspond to the variation of ν in $g_x - g_y$ plane, where we choose the other parameter values for panels (a), (b) are $J = 2.0\Delta_0, \mu = \Delta_0$ and $J = 2.0\Delta_0, \mu = 4.0\Delta_0$ respectively. On the other hand, for panels (c), (d) we choose $J = 4.0\Delta_0, \mu = \Delta_0$ and $J = 4.0\Delta_0, \mu = 4.0\Delta_0$ respectively.

The topological invariant reads [53],

$$\delta = \text{sgn} \prod_{l=1}^4 \det \begin{pmatrix} J + \xi_{\mathbf{k},\mathbf{g}}(\Gamma_l) & \Delta_0 \\ \Delta_0 & J - \xi_{\mathbf{k},\mathbf{g}}(\Gamma_l) \end{pmatrix} = (-1)^\nu, \quad (\text{S4})$$

where the quantity ν is treated as a topological invariant. Therefore, one can identify the topologically trivial and non-trivial regime by considering $\nu = 0$ or $\nu = 1$ accordingly. In Fig.(S1) and Fig.(S2) we illustrate the topological invariant considering symmetric and asymmetric spin spirals (SS) in different parameter regimes. In each figure (Figs. S1 and S2), the yellow region indicates the gapless topological superconducting (TSC) phase ($\nu = 1$) hosting Majorana flat edge modes (MFEM) due to the generation of an effective $(p_x + p_y)$ type of superconducting pairing. On the other hand, in the violet region, the system becomes a topologically trivial gapped superconductor ($\nu = 0$), where MFEM disappear due to the destruction of the $(p_x + p_y)$ type pairing.

S2. METHODOLOGY

In this section, we discuss the computational details for extracting the material specific parameters within *ab initio* electronic structure calculations. All these parameters are for various heterostructures made of an atomic-layer-thick magnetic layer of $3d$ transition metal (TM) elements, Mn and Cr, on the top of normal s -wave superconducting substrate. A body-centred-cubic (*bcc*) Nb with different surface cuts, (110) and (001) is used as the substrate. Ultimately, these parameters are used for generating ground state spin texture by solving extended Heisenberg model within Monte Carlo (MC) simulations [77, 78], which is the essential ingredient for establishing the topological superconducting (TSC) phase.

A. Film geometry relaxation within *ab initio* electronic structure method

We first begin with the optimized lattice of bulk *bcc*-Nb superconductor. The optimized lattice constant of bulk *bcc*-Nb has been obtained by performing first-principles electronic structure calculations within the density-functional theory and the plane-wave pseudopotential approach as implemented in the Vienna Ab-initio Simulation Package (VASP)[86–88]. Exchange and correlation have been considered within the generalized gradient approximation (GGA) which is parametrized via Perdew, Burke, and Ernzerhof (PBE) functional [89]. Here, the projector-augmented wave (PAW) method is employed to construct the pseudopotentials with valence wavefunctions which are approximated smooth near ion cores [90, 91]. The plane wave cut-off energy (500 eV) and the k -point mesh ($16 \times 16 \times 16$ and Γ -centred) in the full Brillouin-zone (BZ) are checked carefully for the BZ integration, ensuring the numerical convergence

of self-consistently determined quantities. The optimised lattice constant of *bcc*-Nb is found to be $a_{\text{opt}}=3.3232 \text{ \AA}$, matching well with the experimental value in the Materials Project database ($a_{\text{expt}}=3.32 \text{ \AA}$) [74].

The surface unit cell (u.c.) in the form of two-dimensional (2D) slab geometry is constructed with sufficiently thick vacuum layers. The thickness of vacuum on each side of the slab is taken about 10 \AA . Assuming a pseudomorphic layer by layer growth, ultrathin magnetic films are constructed by considering a single layer of Mn and Cr on a well known *s*-wave superconductor (SC) substrates Nb(110) and Nb(001), respectively. In case of Mn/Nb(110) film, each surface layer contains two atoms and the thickness of the substrate is taken 11 monolayers (MLs), see Fig. S3(a). In the Cr based film as depicted in Fig. S5(a), one atom per layer is repeated along *c*-axis with the substrate thickness of about 15 MLs. The surface u.c. parameters using optimized *bcc*-Nb lattice constants are $a=3.3232 \text{ \AA}$ with $b/a=\sqrt{2}$ and $a=b=3.3232 \text{ \AA}$ for Mn/Nb(110) and Cr/Nb(001) magnetic films, respectively. Increasing the layer numbers beyond that doesn't carry any effect on the properties of the systems. Later, uniform biaxial strain has been calculated with respect to the optimized lattice constant as, $\text{strain}=\frac{a-a_{\text{opt}}}{a_{\text{opt}}}\times 100\%$. Therefore, the sign of strain in case of expansion (compression) is positive (negative). The number of MLs in the substrate and the vacuum thickness for all film structures with both compressive and tensile strains are kept fixed. We have used the same energy cut-off for the plane waves and the $12\times 8\times 2$ *k*-mesh for the BZ integration. The distances between different layers counting from the top TM layer till the 8th layer (7 interlayer distances) in all films are relaxed until the Hellmann-Feynman force on each atom is smaller than 0.001 eV/\AA . So, we have applied both positive and negative values of strain ($< 5\%$) on both Mn/Nb(110) and Cr/Nb(001) films and relaxed each of them along the growth direction. We find that further relaxation with more layers (> 8) does not change the computed results significantly. In every calculations, the self-consistent energy has been converged with an accuracy of 10^{-7} eV .

In Table I and II, we have provided the theoretical relaxed structure for Mn/Nb(110) and Cr/Nb(001) magnetic films, respectively. The top Mn and Cr layers are assigned with the number $n=0$ in Fig. S3(a) and S5(a), respectively and n increases if one moves down across the film. The relaxed interlayer distances till $n=4$ (first four interlayer separations only) are presented in those Tables and in the parentheses, we provide the changes in % with respect to the ideal interlayer spacing. For example, the ideal interlayer distance in case of Nb(110) and Nb(001) films using the optimized *bcc*-Nb lattice are 2.3499 \AA and 1.6616 \AA , respectively. It is expected that the changes in interlayer distance (in %) will be more with both negative and positive strains. Note, we have carefully checked the optimum numbers (till $n = 6$) of relaxed interlayer distances, beyond that the change in the interested parameters is negligible.

Lattice constant in $\text{\AA}(a_{\text{strain}})$	d_{01} in \AA (% change)	d_{12} in \AA (% change)	d_{23} in \AA (% change)	d_{34} in \AA (% change)
3.432 ($a_{+3.3}$)	1.97(+18.8%)	2.24(+7.7%)	2.24(+7.7%)	2.24(+7.7%)
3.366 ($a_{+1.3}$)	2.00(+16.0%)	2.31(+3.1%)	2.29(+11.4%)	2.30(+11.1%)
3.3232 ($a_{0.0}$)	2.03(+13.5%)	2.35(+0.2%)	2.34(+0.3%)	2.35(+0.2%)
3.270 ($a_{-1.6}$)	2.08(+10.0%)	2.40(-3.8%)	2.42(-4.7%)	2.42(-4.7%)
3.234 ($a_{-2.7}$)	2.10(+8.2%)	2.44(-6.6%)	2.45(-7.0%)	2.44(-6.6%)
3.200 ($a_{-3.7}$)	2.14(+5.4%)	2.47(-9.1%)	2.48(-9.5%)	2.48(-9.5%)

TABLE I. Structural relaxation details for Mn/Nb(110) magnetic film. Here, d_{nm} defines the distance between layers after relaxation. The '+ve' ('-ve') signs in d signifies that relaxed distance is larger (smaller) than the ideal distance in the film, obtained from a in each case.

Lattice constant in $\text{\AA}(a_{\text{strain}})$	d_{01} in \AA (% change)	d_{12} in \AA (% change)	d_{23} in \AA (% change)	d_{34} in \AA (% change)
3.432 ($a_{+3.3}$)	1.22(+28.9%)	1.65(+3.6%)	1.55(+9.8%)	1.6(+6.7%)
3.366 ($a_{+1.3}$)	1.29(+23.4%)	1.67(+0.9%)	1.6(+5.4%)	3.65(+1%)
3.3232($a_{0.0}$)	1.31(+21.07%)	1.68(-1.3%)	1.61(+3.1%)	1.66(0.0%)
3.300($a_{-0.7}$)	1.30(+21.3%)	1.72(-4.2%)	1.63(+0.1%)	1.67(-1.6%)
3.234 ($a_{-2.7}$)	1.36(+15.89%)	1.74(-7.5%)	1.69(-4.6%)	1.71(5.7%)
3.168 ($a_{-4.7}$)	1.38(+12.88%)	1.78(-12.5%)	1.75(-10.6%)	1.73(-9.5%)

TABLE II. Structural relaxation details for Cr/Nb(110) magnetic film. Here, d_{nm} defines the distance between layers after relaxation. The '+ve' ('-ve') signs in d signifies that relaxed distance is larger (smaller) than the ideal distance in the film, obtained from a in each case.

B. Extraction of material specific parameters: Korringa-Kohn-Rostokar Green-function (KKR-GF) method

After the structural relaxation of each magnetic film, the relaxed structures are now used for *ab initio* simulations performed within the scalar-relativistic screened KKR-GF method [92] with exact description of the atomic cells. This method is based on the multiple-scattering theory [94] that consists of dividing the problem in calculating the electronic structure of a solid into two parts: solving a single-site scattering problem for each atom in isolation, then incorporating the structural information of the solid by solving a multiple-scattering problem. Note, all the magnetic films are enclosed by two vacuum regions with a thickness of about 10 Å on both top and bottom sides.

The local spin density approximation (LSDA) has been considered [95]. The effective potentials and fields are treated within the atomic sphere approximation (ASA) with an angular momentum cut-off, $l_{\max}=3$. The energy integrations are performed using a grid of 38 points along a path of the complex-energy contour with a Fermi smearing value of 473 K. For the necessary k integrations in the 2D BZ, we have chosen 1600 ($40 \times 40 \times 1$) k -points in the full surface BZ for the integration of the Matsubara pole closest to the real axis in order to perform the self-consistency. Within KKR-GF method including spin-orbit coupling, we have first converged the potential self-consistently for each film, with confining the magnetic moments along out-of-plane direction (z -direction).

By employing the KKR-GF method, we essentially calculate the following important parameters: the symmetric exchange interaction, \mathcal{J}_{ij} 's, the antisymmetric Dzyaloshinskii-Moriya interaction (DMI), \mathbf{D}_{ij} ($|\mathbf{D}_{ij}| = \mathcal{D}_{ij}$), and the single ion magnetocrystalline anisotropy (MCA), \mathcal{K}_i . These parameters contribute in the following Heisenberg model Hamiltonian described in Eq. (S5) and finally, the numerical solutions within MC simulations describe the magnetic textures in the magnetic layer.

$$\mathcal{H} = - \sum_{i>j} [\mathcal{J}_{ij} \hat{n}_i \cdot \hat{n}_j + \mathbf{D}_{ij} \cdot (\hat{n}_i \times \hat{n}_j)] - \mathcal{K} \sum_i (\hat{n}_i \cdot \hat{z})^2, \quad (\text{S5})$$

where i and j denote the site of atoms in a considered domain and the corresponding \hat{n}_i and \hat{n}_j represent unit vectors along the magnetic moments. In this model, the negative (positive) sign of \mathcal{J} signifies antiferromagnetic (ferromagnetic) pair-wise coupling. This spin Hamiltonian is also describes various topological magnetic states in the presence of external perturbation [79, 80].

The advantage of KKR-GF method is that one can calculate two-site exchange interactions, both isotropic \mathcal{J} and anisotropic \mathbf{D} vector. Here, the non-zero value of DMI with its orientation actually decides the nature of the chiral spin-spiral (SS). Once the converged potential is obtained self-consistently, we perform three single-shot calculations maintaining magnetization along the x, y and z directions and employing the infinitesimal rotations method [93] as implemented within a relativistic generalized formalism [96?]. These allow us to determine all three components of the DMI vector. We took the cutoff radius of seven in unit of the lattice constant ($=7a$ Å) to capture the long-range interactions found in the system. This includes more than 25 intralayer shells for which two-site parameters are extracted. In order to calculate the MCA, the converged potential is further used to calculate the total band energy via one-shot calculations for magnetization oriented along three orthogonal directions (x, y and z). Here, a larger k -point mesh ($80 \times 80 \times 1 = 6400$) is considered. With this consideration, we obtain the MCA as,

$$\mathcal{K}_x = E_x - E_z \text{ and } \mathcal{K}_y = E_y - E_z, \quad (\text{S6})$$

where, positive values of \mathcal{K}_x and \mathcal{K}_y clearly refer to the out-of-plane anisotropy and here, the minimum value between them refers to the single ion MCA constant, \mathcal{K} . The negative value of \mathcal{K} on the other hand refers to the in-plane anisotropy.

C. Numerical calculations for finding the magnetic ground state: Atomistic Spin Dynamics simulations

After extracting all magnetic interaction parameters required for the ground state magnetic textures of Mn/Nb(110) and Cr/Nb(001) systems, we have numerically solved the Eq. S5 within Monte Carlo (MC) simulations [77, 78, 82, 83]. This will give the best atomistic description of our magnetic systems within the Atomistic Spin Dynamics simulations code *Spirit* [76]. The ground state spin textures are found to be robust by means of no change in the ground state configuration with more interaction shells. We performed the simulated annealing process [78] to identify the zero-temperature ground state of the system. In such process, we have considered 10^6 MC steps followed by 10^4 thermalization steps at each temperature step. We started from a finite temperature in the range between 15K and 30 K and reached the zero-temperature ground state configuration with atleast $\times 10^2$ number of steps. A typical size of the simulation domain in our MC simulations is fixed to 32×32 , after carefully checking the ground state configuration in a larger domain of size like 128×128 .

S3. EXAMPLE OF Mn/Nb(110) FILM: OPTIMIZED AND UNIFORMLY PLANAR STRAINED STRUCTURES

A. Mn/Nb(110) film with optimized lattice parameter of *bcc*-Nb

In this subsection of the SM, we first consider a Mn/Nb(110) film in Fig S3(a) constructed with the GGA-optimized lattice parameter of *bcc*-Nb, forming a $c(2 \times 2)$ surface unitcell with lattice constants, $a_{\text{opt}}=3.3232 \text{ \AA}$ and $b_{\text{opt}}=\sqrt{2}a_{\text{opt}}=4.6997 \text{ \AA}$. After relaxation, the calculated exchange parameters, \mathcal{J} and \mathcal{D} , are depicted in Fig. S3(b) as a function of the distance measured in the unit of the smallest surface lattice parameter *i.e.*, a_{opt} . The real distance from an atom at position \mathbf{R}_0 to the other atom at l^{th} neighboring shell can be defined as $|\mathbf{R}_l - \mathbf{R}_0|$. A strong frustration in \mathcal{J} 's is observed in Fig. S3(b) and as a result, we find a $c(2 \times 2)$ antiferromagnet (AFM) as the ground state in our MC simulations, see Fig S3(c). The out-of-plane anisotropy constant is found to be small. A significantly weak DMI strength (the ratio between strongest \mathcal{D} and \mathcal{J} is ≈ 0.02) cannot support any noncollinearity in the $c(2 \times 2)$ -AFM structure. The nearest-neighbor (NN) AFM exchange coupling and the next-nearest-neighbor (NNN) ferromagnetic (FM) exchange coupling with an optimal ratio may support such $c(2 \times 2)$ -AFM phase as the ground state. Indeed, the ground state of Mn/Nb(110) reported in a recent experiment by Conte *et al.* [56] have now been well reproduced within our theoretical model. The simulated spin texture in Fig S3(c) clearly manifests an AFM order along [110] and $[\bar{1}\bar{1}0]$ directions and FM order along [100] and [010] directions.

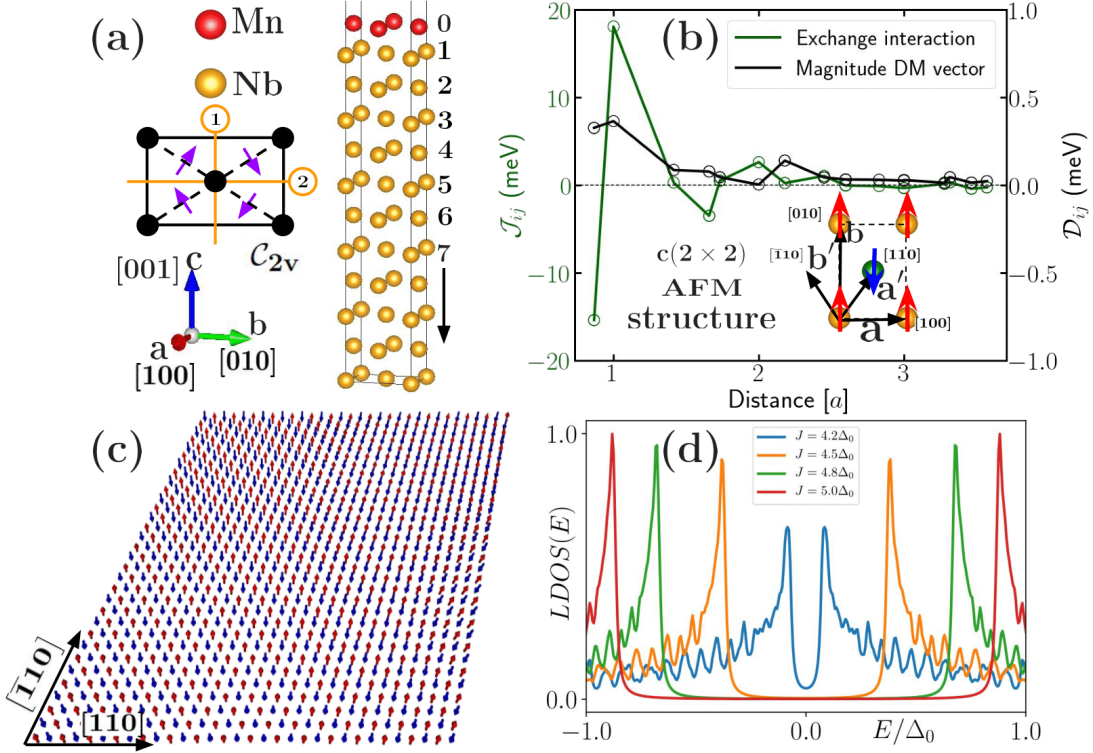


FIG. S3. In panel (a), the unit cell of Mn/Nb(110) used for our *ab initio* calculations. The atoms denoted by red and yellow balls are Mn and Nb atoms, respectively. On the left, the sketch of the rectangular $c(2 \times 2)$ surface u.c. has C_{2v} symmetry with mirror planes ($p=1, 2$) are indicated by yellow lines. The filled black circles represent the surface atoms in the u.c. and the microscopic \mathbf{D} vectors (purple arrows) between NN sites on crystal surface plane are restricted by symmetry to point perpendicular to the bond. Indeed, the calculated vector orientations of all \mathbf{D} vectors in the inset of Fig. 4(a) in the main text follow the C_{2v} symmetry rules [68]. In panel (b), we depict the exchange coupling strength, \mathcal{J}_{ij} and DMI strength, \mathcal{D}_{ij} as a function of distance from a reference atom. The interaction parameters, \mathcal{J} 's and \mathcal{D} 's, till 5th neighbor cell is also presented in Table III. We find the expected decay of both \mathcal{J} and \mathcal{D} with distance $|\mathbf{R}_l - \mathbf{R}_0|$ in units of surface lattice vector a_{opt} . In panel (c), we show an AFM spin texture which is found in the Mn layer within the MC simulation. We have used parameters mentioned in (b) and out-of-plane anisotropy, $\mathcal{K} = 0.04 \text{ meV per Mn atom}$. Panel (d) shows the plot of the local density of states (LDOS) as a function of energy, illustrating the formation of Shiba bands within $\pm\Delta_0$ for the $c(2 \times 2)$ -AFM phase (see the inset of (b)). The exchange field strength J is varied between $4.2\Delta_0$ and $5.0\Delta_0$. We choose $\mu = 4.0\Delta_0, t = \Delta_0$.

A domain of size 32×32 has been used for solving Eq. (4) in the main text and the obtained results are summarized in Fig. S3(d), describing the local density of states (LDOS) as a function of energy (E). Due to the overlapping of the Yu-Shiba-Rusinov (YSR) in-gap bound states, the Shiba bands are formed within the superconducting gap $\pm\Delta_0$. We further vary the coupling constant J between the local magnetization (in the Mn spin texture) and the itinerant spin (free electrons in the SC) to ensure the trivial superconductivity in the system. Precisely, a proximity induced SC sustains in the AFM Mn layer. Based on our results from our model (Eq. (4) in the main text), we can firmly reproduce the experimental findings *i.e.*, the coexistence of SC and AFM phases [56].

B. Role of uniform biaxial surface strain for AFM-SS ground state in Mn/Nb(110) film

Here, we discuss a transition to an AFM-SS state from the $c(2 \times 2)$ state in the top Mn layer of Mn/Nb(110) heterostructure by applying an uniform biaxial strain in the 2D film geometry. As the strain changes the in-plane lattice parameters keeping $b=\sqrt{a}$ unaltered, the relaxed film is expected to change \mathcal{J} 's, \mathcal{D} 's and \mathcal{K} value for the magnetic layer. In Table III, we have presented various quantities calculated within KKR-GF method while the Fig. S4(a) depicts the effect of strains on \mathcal{J} 's as a function of distance between Mn atoms. In the second column of the Table III, the magnetic moment of Mn within KKR-GF calculation is matching well with that of obtained from VASP relaxation calculations. The plot in Fig. S4(a) ensures the strong frustration in \mathcal{J} 's even after varying the planar strain from tensile (positive) to compressive (negative). Indeed, the dominating parameters are the Heisenberg exchange parameters and the first two \mathcal{J} 's are the strongest in comparison to the rest. In particular, the NN exchange constant ('-ve' means AFM) is gradually increasing in magnitude with changing strain from tensile to compressive while the trend is opposite in case of NNN ('+ve' means FM) exchange constant except for $a_{+3.3}$ case, see Table III.

Interestingly, this strong exchange frustration has adverse effect in the ground state magnetic phase of Mn/Nb(110), although, the $c(2 \times 2)$ -AFM phase remains the lowest energy magnetic configuration under the tensile strain *i.e.*, when the 2D surface u.c. is expanded. An AFM-SS state becomes the lowest energy ground state under a small compressive strain of magnitude 1.6 %. It is worth to mention that such AFM-SS ground state is rarely found in film geometry and the number of examples is very limited [59]. Here, this SS state in Fig. S4(c) can be stabilized by the exchange frustration even in the presence of small out-of-plane \mathcal{K} . We further increases the compressive strain and the AFM-SS solution is found with a small variation in the period λ_{Mn} for strains -2.7% and -3.7% both. We find that the AFM-SS state exists for a delicate balance between NN AFM and NNN FM \mathcal{J} values, hardly affected by the rest of isotropic exchange interaction terms. The spin spiral presented in Fig. S4(c) for -2.7% strain has a period of about $\lambda_{\text{Mn}} \approx 2.82$ nm computed using MC simulations. In such cases, the sense of rotation of the SS will have degeneracy which generally breaks in the presence of chiral interactions *i.e.*, the DMI. Hence, using the full Hamiltonian in Eq. (S5), we have identified a right-handed cycloidal AFM-SS state, see Fig. S4(b) and also Fig. 4(b) in the main text. Comparing (b) and (c), we find that even relatively weak DMI strength changes the period of the SS to an expected lower value, $\lambda_{\text{Mn}} \approx 2.35$ nm, propagating along [010] direction. In contrast, the AFM-SS earlier reported in Mn/W(110), a non-SC film system, where a strong DMI determines the left-rotating spin cycloid, owing to the strong SOC from the heavy metal element W [59].

The exchange frustration driven AFM-SS is now examined by numerically solving Eq. (4) in the main text. A 32×32 domain as presented in Fig. S4(d) is considered for the spin-lattice model and the corresponding result, particularly the LDOS for the zero-energy ($E = 0$) is depicted in Fig. S4(e). The zero-energy states are indeed localized at the edges of the considered magnetic domain while the bulk YSR band is semimetallic. Therefore, this AFM-SS can give rise to MFEM mode (see Fig. S4(e)), even without DMI. Akin to the main text (see inset of Fig. 5(a)), non-dispersive states at the zero-energy is also observed in the eigenvalue spectrum. In general, the antisymmetric DMI term in magnetic films with broken inversion symmetry is the result of an indirect exchange mechanism in the presence of spin-orbit coupling (SOC) present in the substrate elements [68, 75, 98]. In many 2D magnetic systems, this plays an important role in stabilizing SS state which otherwise does not appear with the exchange interactions only [58]. This is also true in case of Mn/Nb(110) with optimized lattice constant, see the subsection S3 A. Hence, for Mn/Nb(110) magnetic film, strain is an important controlling parameter to stabilize the AFM-SS state and hence, triggers the TSC phase. Comparing the results presented in the main text Fig. 5(a)-(b) and Fig. S4(e), we have established that the TSC phase transition from a trivial state can occur when the noncollinear spin textures in the form of SS becomes a stable solution in a transition-metal/superconductor (TM/SC) heterostructure even in the absence of DMI, a SOC driven interaction parameter.

Lattice constant in Å (a_{strain})	Magnetic mom. \mathcal{M}_{Mn} in μ_{B} KKR-GF, (VASP)	MCA \mathcal{K} in meV/Mn	DMI magnitude in meV				Isotropic exchange interaction (meV)					Ground state spin texture
			\mathcal{D}_{01}	\mathcal{D}_{02}	\mathcal{D}_{03}	\mathcal{D}_{04}	\mathcal{J}_1	\mathcal{J}_2	\mathcal{J}_3	\mathcal{J}_4	\mathcal{J}_5	
3.432 ($a_{+3.3}$)	3.63, (3.51)	0.22	0.53	0.5	0.02	0.05	-12.41	17.96	2.78	-2.6	1.25	AFM
3.366 ($a_{+1.3}$)	3.57, (3.46)	0.17	0.42	0.52	0.04	0.07	-14.44	18.84	1.34	-3.18	0.78	AFM
3.3232 ($a_{0.0}$)	3.56, (3.43)	0.04	0.33	0.37	0.09	0.08	-15.38	18.01	0.03	-3.49	0.5	AFM
3.270 ($a_{-1.6}$)	3.55, (3.43)	0.22	0.28	0.19	0.14	0.07	-16.58	16.16	-0.57	-3.38	0.15	AFM-SS
3.234 ($a_{-2.7}$)	3.53, (3.39)	0.22	0.28	0.11	0.2	0.07	-17.89	15.37	-0.86	-3.26	0.17	AFM-SS
3.200 ($a_{-3.7}$)	3.52, (3.40)	0.29	0.28	0.04	0.27	0.05	-19.61	14.49	-0.67	-2.96	0.3	AFM-SS

TABLE III. The first three columns provide the smallest lattice constants under strain, \mathcal{M}_{Mn} obtained from both KKR-GF and VASP for each Mn atom and single ion MCA constant (all are out-of-plane), respectively. Next, the \mathcal{D}_{0j} and \mathcal{J}_i for first few neighboring cells are tabulated. The different lattice constants signify the system is constructed with different uniform biaxial strain values: from top to bottom, tensile 3.3% ($a_{+3.3}$), tensile 1.3% ($a_{+1.3}$), optimized 0.0% ($a_{0.0}$), compressive 1.6% ($a_{-1.6}$), compressive 2.7% ($a_{-2.7}$), and compressive 3.7% ($a_{-3.7}$). The strains are calculated with respect to the optimised lattice constant, $a_{\text{opt}}=3.3232$ Å. The last column clearly indicates a transition from a collinear AFM state to a noncollinear AFM-SS state under a small compressive strain.

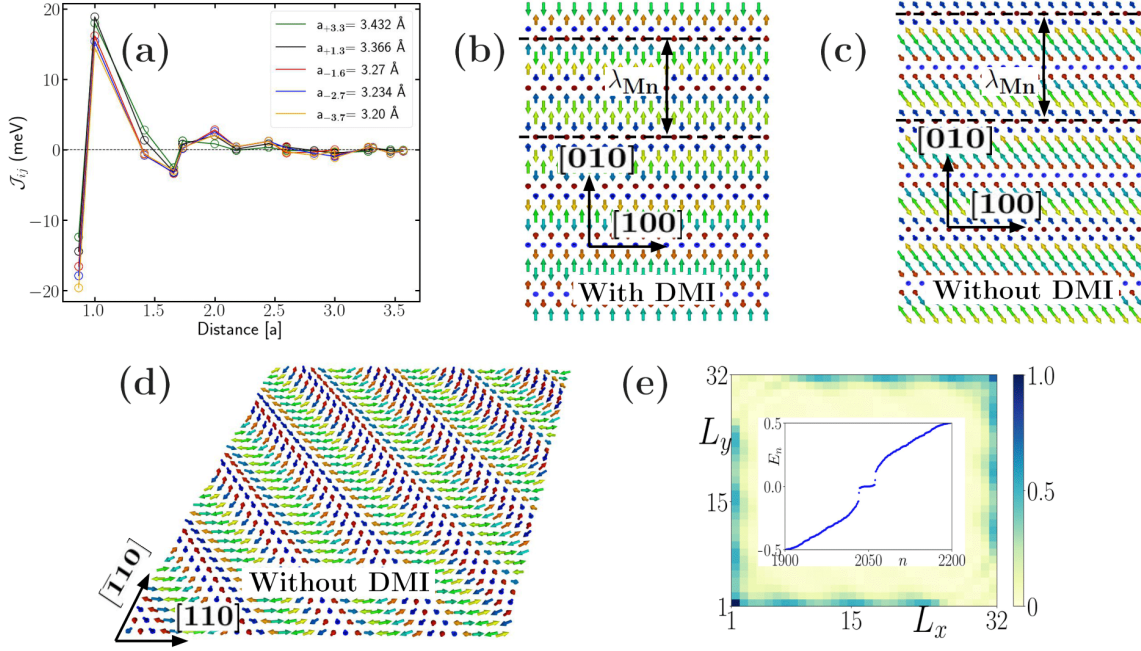


FIG. S4. For various strain values, in panel (a) we depict \mathcal{J} 's as a function of distance. Spin textures in panels (b) and (c) illustrate the ground state AFM-SS solutions with DMI and without DMI, respectively. The magnitude of the compressive strain is fixed to 1.6. The AFM-SS state becomes an homogeneous right-handed AFM cycloid in the presence of DMI, propagating along $[010]$ direction and the spins are rotated in the yz -plane. (d) An AFM-SS domain is constructed from the spin texture shown in panel (c) and hence edges of the domain are $[110]$ and $[\bar{1}10]$. The normalized LDOS corresponding to $E=0$ eigenstate is shown in panel (d) in the L_x - L_y square plane. The inset depicts the corresponding eigenvalue spectrum E_n as a function of the state index n . Hence, clearly we obtain TSC phase hosting MFEM in the absence of DMI. Here, we choose $\mu = 4.0\Delta_0$, $t = \Delta_0$ and $J = 1.5\Delta_0$.

S4. EXAMPLE OF Cr/Nb(001) FILM: OPTIMIZED AND UNIFORMLY PLANAR STRAINED STRUCTURES

This section deals with another promising prototype candidate, a single layer Cr on Nb(001) substrate, see Fig. S5(a). To the best of our knowledge, no study has been conducted so far on this ultrathin magnetic film sample. The optimized

Cr/Mn(001) film exhibits a noncollinear spin texture which is a different type of AFM-SS. Interestingly, the SS ground state is found without any strain. However, we follow the same approach for this system like in Mn/Nb(110) film. In contrast to the Mn/Nb(110) surface u.c., here the surface u.c. possesses square geometry which has C_{4v} symmetry.

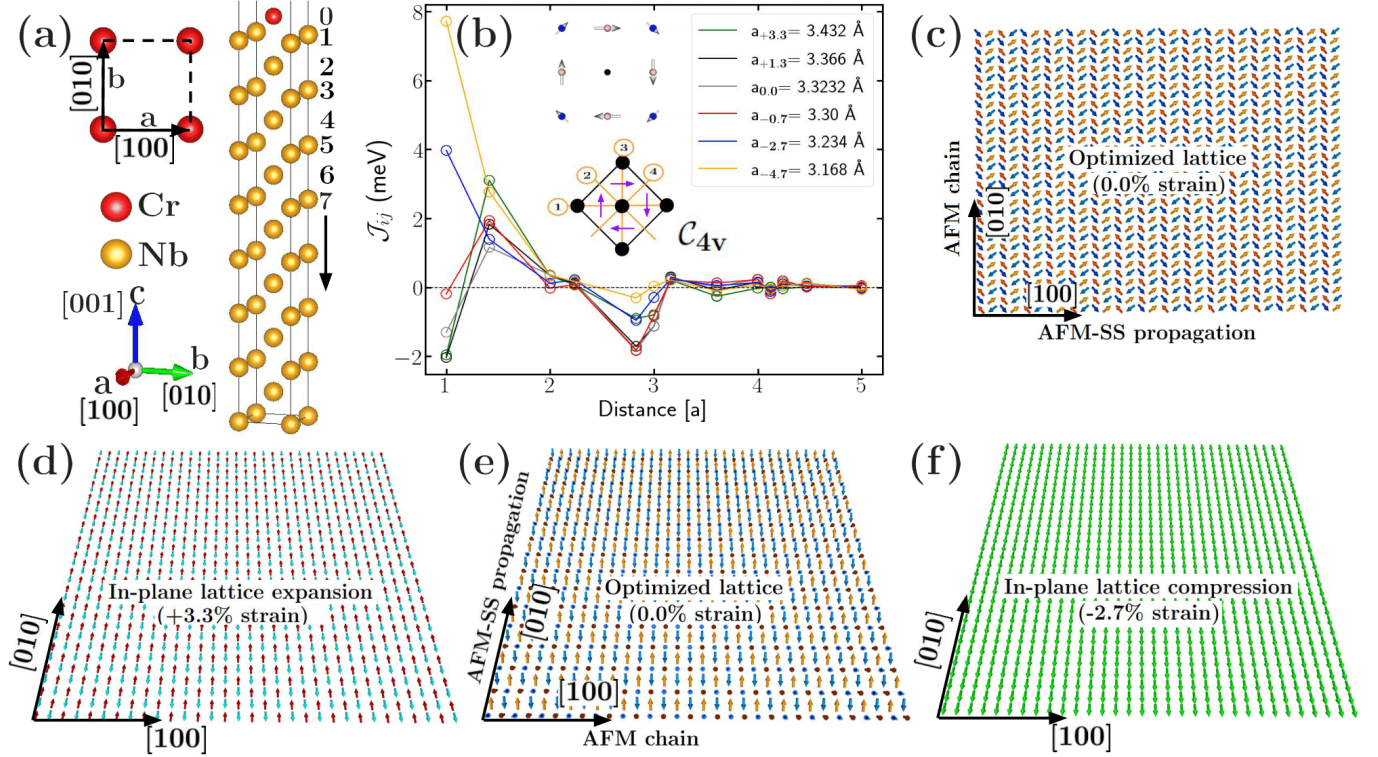


FIG. S5. In panel (a), we present the unit cell of Cr/Nb(001). The atoms denoted by red and yellow balls are Cr and Nb atoms, respectively. The usual J'_{ij} 's are plotted in panel (b) as a function of distance and the top figure in the inset shows the orientation of NN and NNN DM vectors for the film constructed with optimized lattice constant of Nb. Here, the calculated \mathbf{D} vectors are shown on the atoms instead of bonds connection NN and NNN atoms. Below, the sketch of a square surface lattice describing the C_{4v} symmetry and the mirror planes ($p=1$ to 4) are depicted by yellow lines. The filled black circles represent the surface atoms in the lattice and the microscopic NN \mathbf{D} vectors (purple arrows) on the crystal surface plane respects the symmetry to point perpendicular to the bond. This is indeed matching with the Moriya rules for C_{4v} symmetric system [68]. Panel (c) represents the spin texture with interchanging the [100] and [010] directions. In panels (d), (e) and (f), we demonstrate the evolution of the spin textures driven by the strain parameter. They correspond to the in-plane ferromagnetic (with tensile +3.3% strain), AFM-SS (with zero strain) and in-plane AFM spin texture (with compressive -3.7% strain) respectively.

In Fig. S5(b), we illustrate the behavior of J_{ij} 's under different strain values and the inset describes the orientation of DMI vectors. Note that, following the C_{4v} symmetry present in the system, the orientation of DMI vectors around a Cr atom are perpendicular to the bond connecting NN and NNN Cr atoms [68]. As we keep increasing the strain starting from 3.3 % tensile, we observe that the NN exchange interaction changes sign *i.e.*, a weak AFM coupling becomes a strong FM coupling, see the exchange interaction part in Table IV. On the other hand, the next dominating exchange constant, the NNN one remains FM for all values of strain. The \mathcal{D} is small here too, owing to the weak SOC strength in Nb. However, compared to Mn/Nb(110) film, the exchange constants are found to be relatively weak. Interestingly, in contrast to Mn/Nb(110), the MCA constants are all in-plane, see the third column in Table IV. A strong variation in \mathcal{J} 's under strain makes Cr/Nb(001) film an exciting playground for tailoring magnetism.

Indeed, in Figs. S5(d)-(f), with varying strain, we show that the in-plane AFM ground state for the expanded surface u.c. changes to an in-plane FM ground state under compression. Surprisingly, a noncollinear spin texture (AFM-SS) appears as the ground state with the optimized lattice geometry ($a_{\text{opt}} = 3.3232 \text{ \AA}$). This particular AFM-SS in Fig. S5(e) exhibits an AFM chain along [100] direction and spins are rotating in the yz -plane. So, the AFM-SS is propagating along [010] direction with the sense of spin rotation left-handed (left-handed cycloid). Here, the period of the spiral is small compared to that of Mn/Nb(110), $\lambda_{\text{Cr}} \approx 1.33 \text{ nm}$. This is due to the fast rotation of spins along [010] direction. Here, the interplay between relatively weak, both \mathcal{J} 's and \mathcal{D} 's stabilizes the SS even in the presence of small in-plane anisotropy. Respecting the C_{4v} symmetry, the chiral AFM-SS ground state is found to be degenerate

in our simulation. The texture in Fig. S5(c) represents another AFM-SS state where the AFM chain along the [010] direction rotates in the xz -plane and hence, the propagation direction is [100].

Lattice constant in Å (a_{strain})	Magnetic mom. \mathcal{M}_{Cr} in μ_{B} KKR-GF, (VASP)	MCA \mathcal{K} in meV/Cr	DMI magnitude in meV				Isotropic exchange interaction (meV)					Ground state spin texture
			\mathcal{D}_{01}	\mathcal{D}_{02}	\mathcal{D}_{03}	\mathcal{D}_{04}	\mathcal{J}_1	\mathcal{J}_2	\mathcal{J}_3	\mathcal{J}_4	\mathcal{J}_5	
3.432 ($a_{+3.3}$)	2.78, (2.83)	-0.40	0.32	0.02	0.02	0.1	-1.96	3.1	0.32	0.07	-0.91	In-plane AFM
3.366 ($a_{+1.3}$)	2.96, (2.84)	-0.41	0.60	0.29	0.03	0.09	-2.04	1.83	0.34	0.12	-1.72	In-plane AFM
3.3232 ($a_{0.0}$)	2.69, (2.81)	-0.37	0.85	0.51	0.001	0.05	-1.31	1.16	0.36	0.15	-1.82	AFM-ss
3.300 ($a_{-0.7}$)	2.69, (2.62)	-0.37	0.89	0.58	0.02	0.05	-0.19	1.93	-0.03	0.08	-1.84	AFM-ss
3.234 ($a_{-2.7}$)	2.79, (2.55)	-0.28	0.97	0.46	0.15	0.14	3.97	1.39	0.11	0.22	-0.96	In-plane FM
3.168 ($a_{-4.7}$)	2.38, (2.36)	-0.28	0.7	0.31	0.11	0.15	7.72	2.76	0.33	0.17	-0.31	In-plane FM

TABLE IV. The first three columns provide the surface lattice constant under strain, \mathcal{M}_{Cr} obtained from both KKR-GF and VASP in the parenthesis and single ion MCA constant (all are in-plane), respectively. Next, the \mathcal{D}_{0j} and \mathcal{J}_i for first few neighboring cells are tabulated. The different lattice constants signify the system is constructed with different uniform biaxial strain values: from top to bottom, tensile 3.3% ($a_{+3.3}$), tensile 1.3% ($a_{+1.3}$), optimized 0.0% ($a_{0.0}$), compressive 1.6% ($a_{-0.7}$), compressive 2.7% ($a_{-2.7}$), and compressive 4.7% ($a_{-4.7}$). The strains are calculated with respect to the optimized lattice constant, $a_{\text{opt}}=3.3232$ Å. The last column clearly indicates a transition from an in-plane AFM state to an in-plane FM state via a noncollinear AFM-SS state.

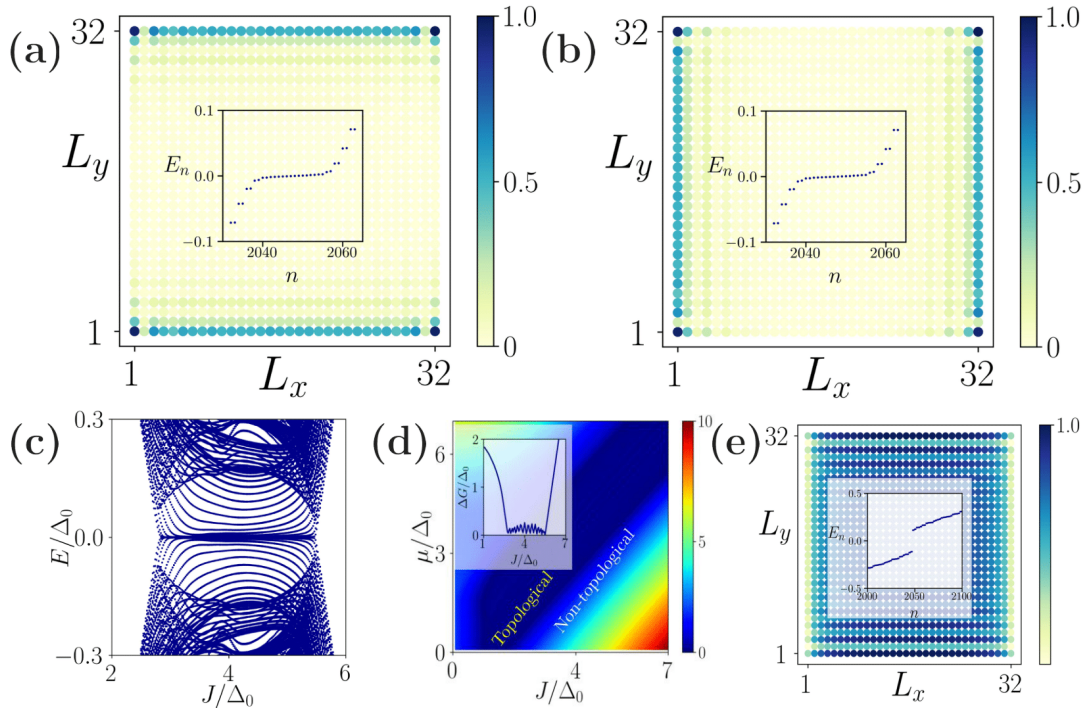


FIG. S6. By using a square domain within L_x - L_y plane, in panels (a) and (b) we depict the normalized LDOS for $E = 0$ states at $J = 3.5\Delta_0$, indicating the MFEM at parallel edges along (100) direction (Fig. S5(c), the corresponding spin texture) and parallel edges along (010) direction (Fig. S5(e), the corresponding spin texture), respectively. Insets show the eigenvalue spectrum E_n as a function of the state index n . (c) The energy eigenvalues E of the Hamiltonian H (Eq. (4) in the main text) is plotted as a function of the exchange coupling constant J employing open boundary condition. We choose $\mu = 4.0\Delta_0$ and $\Delta_0 = t$. (d) The bulk-gap ΔG profile in the J - μ plane is shown by employing the periodic boundary condition. The dark (light) blue regime represent the TSC phase (non-TSC phase). In the inset plot, we demonstrate the ΔG as function of J for a fixed $\mu(= 4.0\Delta_0)$ for more clarity. (e) The trivial phase occurs for $J = 5.5\Delta_0$ and the eigenvalue spectrum E_n as a function of the state index n clearly shows a gap at $E=0$.

Now, based on the solutions obtained from the spin lattice model (Eq. (5) in the main text), Figs. S6(a) and (b)

describe the LDOS behavior for $E=0$ in the L_x - L_y plane for domains with spin textures shown in Fig. S5(c) and Fig. S5(e), respectively. Note, here we consider the spin texture in a domain that is the key ingredient in stabilizing the TSC phase. One can clearly find the edges where localization of the $E = 0$ state occurs and in both cases the TSC phase is identified. Additionally, the parallel edges where we find the localized non-dispersive MFEM, strongly depend on the nature of the SS. Particularly, in the present case, the degenerate AFM-SS ground states both stabilize the MFEM on the two parallel edges and depending on the propagation direction, edges are orthogonal to each other, compare Fig. S5(c) (corresponding LDOS in Fig. S6(a)) and Fig. S5(e) (corresponding LDOS in Fig. S6(b)). Furthermore, the signature of non-dispersive MFEM is more convincing from the low-lying states (at $E_n = 0$) in the eigenvalue spectrum, E_n as a function of the state index n , presented in the insets of Figs. S6(a) and (b). It is worth to mention that in real experiments, such magnetic domain in general possesses both degenerate solutions [99] *i.e.*, [100] and [010] propagating SSs together in a single AFM-SS domain and hence, one should expect the MFEM on any edge of a square domain. The calculations are done with exchange coupling strength $J = 3.5\Delta_0$. On the other hand, in case of $J = 5.5\Delta_0$ (see Fig. S6(e)), the system becomes topologically trivial. One can identify the disappearance of the MFEM from the LDOS (at $E = 0$) distribution in Fig. S6(e) and also, the gapped eigenvalue spectrum in the inset. Thus, the appearance of the MFEM from the real material-based study supports our theoretical proposal, see Fig. 3(c) in the main text.

We depict the energy eigenvalue spectrum (E/Δ_0) as a function of J/Δ_0 employing open boundary condition in Fig. S6(c). In comparison to that of Mn/Nb(110) (see Fig. 5(c)), the gapless TSC phase hosting MFEM appears in a wider range of J , between $3.5\Delta_0$ to $5.3\Delta_0$. To further identify the parameter regime, particularly in the μ - J plane, in which the MFEM appears, we further investigate the bulk-gap $\Delta G = |E_2 - E_1|$ employing periodic boundary condition. Here, E_1 and E_2 represent the two lowest YSR bands. We depict $\Delta G/\Delta_0$ in the J/Δ_0 - μ/Δ_0 plane in Fig. S6(d), see also Fig. 5(d) in the main text for Mn/Nb(110). Here, the gapless TSC regime is also highlighted by the dark blue strip where $\Delta G \simeq 0$ and the regime outside ($\Delta G > 0$) represents the trivial superconducting phase. In the inset of Fig. S6(d), we illustrate the bulk-gap ΔG as function of J for a fixed value of the chemical potential μ , for further transparent visibility of the TSC regime. The bulk-gap ΔG vanishes in the topological regime ($\sim 3.5\Delta_0$ to $5.3\Delta_0$) and MFEM appears at the boundary (edges of the sample).

In compared to the Mn/Nb(110) example in the main text and here, for Cr/Nb(001) example we find that the location of the MFEM depends on the propagation direction of the SS. So, owing to the C_{4v} symmetry in the surface unit cell of Cr/Nb(001), the MFEM can be probed experimentally at any edge of a square domain which generally contains both propagating SSs.

The localized nondispersive MFEMs, extending along a 1D spatial dimension, observed on the two parallel edges as in Figs. S6(a) and (b) appear to be highly tunable with the magnetic texture. Our model's unique TSC features open up the possibility of exploring alternating braiding operations in 2D, offering an alternative approach to the conventional zero-dimensional quasiparticles such as Majorana zero modes (MZMs) typically found in 1D systems [3?]. The presence of controllable underlying magnetic textures enables a highly tunable topological phase, potentially leading to the confinement and transport of MFEM in 2D systems. An intriguing possibility is to engineer a 2D system to create an arrangement of MFEMs selectively localized on the edges of finite domains. Indeed, this concept shares similarities with the idea of braiding Majorana bound states in a magnetic tunnel junction array [?]. Although our model provides a promising platform for manipulating and realizing MFEM in real TM/SC examples, the non-Abelian braiding statistics remain a challenging aspect for next-level topological quantum operations in 2D. Despite the challenges in implementing non-Abelian braiding statistics for MFEM, it can be possible to engineer the edge modes in a manner that allows the injection of a pair of edge vortices into the system. Braiding of an edge vortex might be achievable when it crosses the branch cut of a bulk vortex. In a similar context, a Josephson junction geometry has been explored to inject isolated vortices into chiral edge channels in 2D [?]. However, it is essential to carefully investigate whether the injection of vortices is feasible through flat Majorana edge modes, particularly in the case of vanishing group velocity. Another device proposal in 2D involves a junction of Quantum Anomalous Hall Insulator (QAHI) and topological superconductor (TS) layers, where a properly designed QAHI-TS-QAHI junction [?] could serve as an implementation of topologically protected quantum gates. Our model, featuring nondispersive MFEMs, distinguishes itself from existing 2D examples that primarily rely on chiral dispersive edge modes in various proposals. Nevertheless, to fully understand the potential for braiding operations and non-Abelian statistics with nondispersive MFEMs, further investigation and new developments are required.

In summary, these studies with a wide variation in noncollinear AFM spin textures firmly establish the non-trivial TSC phase hosting MFEM, allowing a formal connection between noncollinear magnetism in real materials and model studies.

S5. YSR/SHIBA ENERGY BAND FORMATION DUE TO THE AFM-SS STATE IN THE MN LAYER ON TOP OF Nb(110) SURFACE

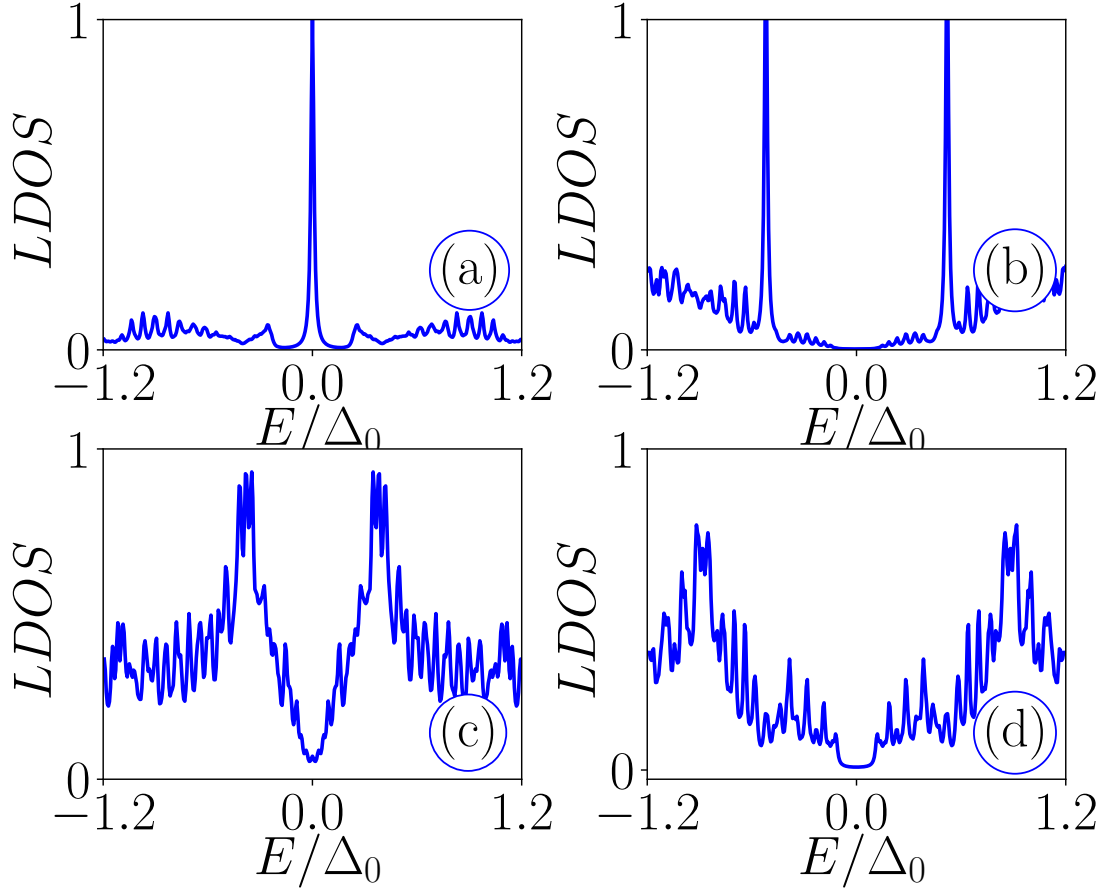


FIG. S7. Panels (a), (b) correspond to the behavior of LDOS as a function of E/Δ_0 for two different values of exchange coupling strength $J = 4.5\Delta_0$ and $J = 5.0\Delta_0$ respectively, when we measure LDOS at the edge of the system. Panels (c), (d) indicate the formation of Shiba bands at the same parameter values when we measure LDOS at the middle of the system.

In this section of the SM, we discuss about the non-topological Shiba band formed within the energy scale $E = \pm\Delta_0$ in the presence of Mn layer as magnetic impurities (AFM-SS) placed on top of an s -wave superconductor Nb (110). We obtain the signature of Shiba band when we compute LDOS at the middle of the system. These Shiba bands play the pivotal role during the topological phase transition.

In Fig. S7(a), we obtain a sharp peak at $E = 0$ in the LDOS behavior for $J = 4.5\Delta_0$. This is a signature of the MFEM (topologically non-trivial) when calculated at the edges of the system. On the other hand, in Fig. S7(c) we depict the corresponding YSR (or simply Shiba) band features in LDOS with the same exchange coupling value $J = 4.5\Delta_0$, when we compute LDOS at the middle of the system. The semimetallic behavior arising in the LDOS [see Fig. S7 (c)] is the signature of the gaplessness (graphene-like behavior) of the bulk YSR band in the topological regime. This is consistent with the Fig. 2(d) (blue curve) in the main text. On the other hand, Fig. S7(b) and Fig. S7(d) represent LDOS at the edge and middle (YSR/Shiba band) of the system respectively in the non-topological regime (when $J = 5.0\Delta_0$), where MFEM peak disappears at the edges, see Fig. S7(b). Concomitantly, LDOS in Fig. S7 (d) exhibits a gapped superconductor instead of a semimetallic phase. Similarly, in Fig. S8, panels (a), (b), (c), (d) correspond to the spatial variation of the LDOS at finite energy $E = 0.1\Delta_0$ in the L_x - L_y plane for four different values of the exchange coupling strength $J = 4.0\Delta_0, 4.2\Delta_0, 4.5\Delta_0, 5.0\Delta_0$ respectively. One can observe a significant variation of the non-topological Shiba bands for each case due to the presence of the Mn layer as magnetic SS.

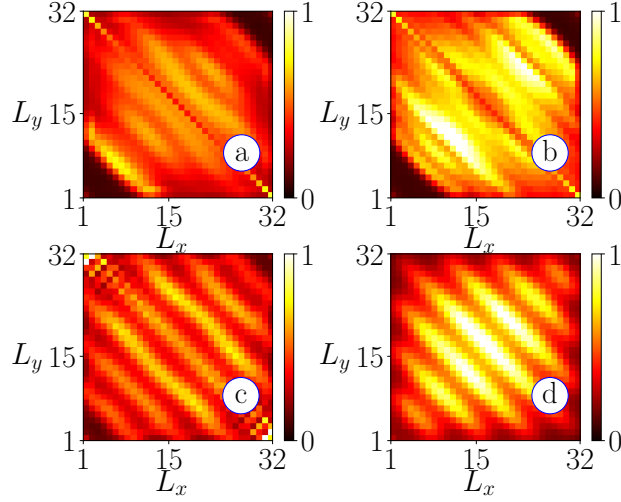


FIG. S8. Panels (a), (b), (c), (d) correspond to the variation of LDOS at finite energy $E = 0.1\Delta_0$ in L_x - L_y plane (highlighting corresponding features of YSR band) with respect to the exchange field strength $J = 4.0\Delta_0, 4.2\Delta_0, 4.5\Delta_0, 5.0\Delta_0$ respectively.

S6. DERIVATION OF AN EFFECTIVE p -WAVE SUPERCONDUCTING PAIRING

In the following section, we investigate the characteristics of the effective pairing mechanism [84, 85] that leads to the formation of the gapless topological superconducting phase in 2D, hosting nondispersive MFEM in our model. Our analyses begin with the consideration of the effective \mathbf{k} -space model,

$$\tilde{H}(\mathbf{k}) = \xi_{\mathbf{k},\mathbf{g}}\tau_z + \frac{1}{2}\mathbf{g}\cdot\mathbf{k}\sigma_z\tau_z + J\sigma_x + \Delta_0\tau_x. \quad (\text{S7})$$

This is also presented in Eq. (3) in the main text of our study, where all terms are appropriately defined. The Bogoliubov de-Gennes (BdG) form of the above Hamiltonian reads,

$$\tilde{H}(\mathbf{k}) = \begin{pmatrix} \xi_{\mathbf{k},\mathbf{g}}\sigma_0 + J\sigma_x + \frac{1}{2}\mathbf{g}\cdot\mathbf{k}\sigma_z & \Delta_0\sigma_0 \\ \Delta_0\sigma_0 & -\xi_{\mathbf{k},\mathbf{g}}\sigma_0 + J\sigma_x - \frac{1}{2}\mathbf{g}\cdot\mathbf{k}\sigma_z \end{pmatrix}, \quad (\text{S8})$$

where, $\xi_{\mathbf{k},\mathbf{g}} = \frac{1}{2}(k_x^2 + k_y^2 + \mathbf{g}^2) - \mu$, $\mathbf{k} = (k_x, k_y)$ and $\mathbf{g} = (g_x, g_y)$. We assume that $g_x = g_y = g$. In our quest to establish a dual representation for the BdG Hamiltonian, as described in Eq. (S8), we aim to find an equivalent dual Hamiltonian denoted as $\tilde{H}^D(\mathbf{k})$. In this process, we utilize a unitary operator responsible for the duality transformation. We define the selected unitary operator for this purpose as follows:

$$S = \frac{1}{\sqrt{2}} \begin{pmatrix} 1_{2\times 2} & 1_{2\times 2} \\ 1_{2\times 2} & -1_{2\times 2} \end{pmatrix}. \quad (\text{S9})$$

By this unitary transformation, the Hamiltonian becomes,

$$\tilde{H}^D(\mathbf{k}) = S^\dagger \tilde{H}(\mathbf{k}) S. \quad (\text{S10})$$

Hence, the equivalent dual Hamiltonian can be written as,

$$\tilde{H}^D(\mathbf{k}) = \begin{pmatrix} \epsilon_{\mathbf{k}}^D\sigma_0 + J\sigma_x & \tilde{\Delta}^D(\mathbf{k})\sigma_0 \\ \tilde{\Delta}^D(\mathbf{k})\sigma_0 & -\epsilon_{\mathbf{k}}^D\sigma_0 + J\sigma_x \end{pmatrix}, \quad (\text{S11})$$

where,

$$\begin{aligned} \epsilon_{\mathbf{k}}^D &= \Delta_0, \\ \tilde{\Delta}^D(\mathbf{k}) &= \frac{1}{2}g(k_x + k_y)\sigma_z + \xi_{\mathbf{k},\mathbf{g}}\sigma_0. \end{aligned} \quad (\text{S12})$$

At low energy limit ($k_x, k_y \sim 0$), keeping the linear order of k_x and k_y , the effective pairing takes the form,

$$\tilde{\Delta}^D(\mathbf{k}) \simeq \left(\mu - \frac{g^2}{2} \right) \sigma_0 + \frac{g}{2} (k_x + k_y) \sigma_z. \quad (\text{S13})$$

In case of spin up ($\uparrow\uparrow$) and spin down ($\downarrow\downarrow$) channel dual pairing becomes,

$$\tilde{\Delta}_{\uparrow/\downarrow}^D(\mathbf{k}) = \left(\mu - \frac{g^2}{2} \right) \pm \frac{g}{2} (k_x + k_y). \quad (\text{S14})$$

Thus, it is evident that the spin-orbit coupling term ($\frac{1}{2}\mathbf{g}\cdot\mathbf{k}\sigma_z$), arising from the spin spiral in the original Hamiltonian $\tilde{H}(\mathbf{k})$, is formally transformed into an effective “ $p_x + p_y$ -type” pairing with a constant kinetic energy term $\epsilon_{\mathbf{k}}^D = \Delta_0$ in the dual Hamiltonian. This intriguing result suggests that the signature of the topological superconducting phase, namely the nondispersive MFEM, arises due to a unique p -wave pairing mechanism resulting from the interplay between the spin-spiral state and the normal s -wave superconductivity. The unitary transformation S , which is independent of \mathbf{k} , does not alter the topological invariant, ensuring the topological equivalence between Eq. (S8) and Eq. (S11).

S7. EFFECT OF RASHBA SOC ON SINGLE-ORBITAL MODEL AND AN EXTENSION TO MULTI-ORBITAL THEORY

In the presence of single-orbital (SO) channel, Rashba SOC term becomes [49],

$$H_{\text{SO}}^R = \lambda_R \tau_z (\sigma_x \sin k_y - \sigma_y \sin k_x), \quad (\text{S15})$$

where λ_R is the Rashba SOC strength. Here, the Pauli matrices σ and τ operate on the spin and particle-hole degrees of freedom, respectively. Similarly, in the presence of multi-orbital (MO) channels the same term [Eq. (S15)] added in the Hamiltonian [Eq. (4) in the main text] takes the form [64, 65],

$$H_{\text{MO}}^R = \lambda_R \tau_z \Gamma_{\text{orb}} (\sigma_x \sin k_y - \sigma_y \sin k_x), \quad (\text{S16})$$

where, $\Gamma_{\text{orb}} = \begin{pmatrix} 1 & 0 \\ 0 & 0 \end{pmatrix}$ represents orbital degrees of freedom. Therefore, we study the effect of MO and SOC on prototype heterostructures where the magnetic layer is based on 3d-transition metal (TM) element deposited on the s -wave superconducting (SC).

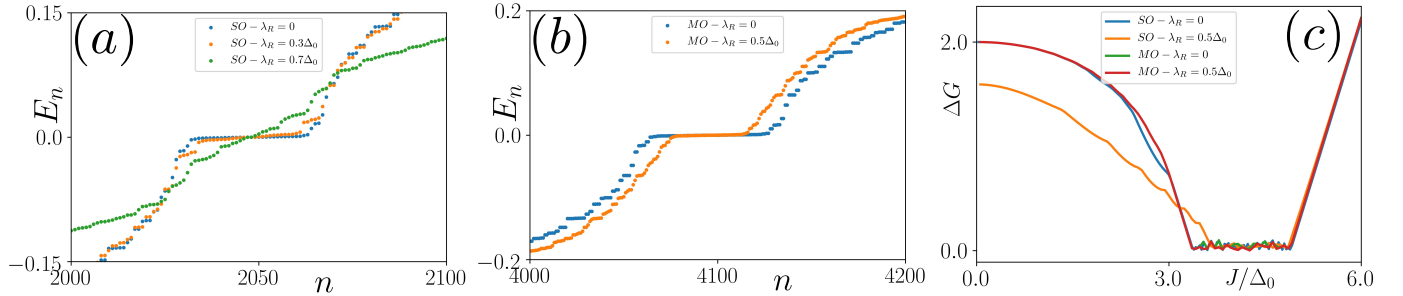


FIG. S9. Panels (a) and (b) depict the eigenvalue spectra of the lattice Hamiltonian containing SO and MO channels, respectively. Here, we have varied the Rashba SOC strength, λ_R , while using an open boundary condition in the 2D finite domain. The lattice model takes into account the noncollinear spin texture in the form of AFM-SS (strained Mn/Nb(110) system). The exchange coupling strength is chosen as $J = 4.5\Delta_0$ for all cases. Panel (c) illustrates the bulk gap as a function of the exchange coupling strength, while considering periodic boundary conditions in 2D. We investigate four different scenarios: (i) SO without Rashba SOC, (ii) SO with Rashba SOC, (iii) MO without Rashba SOC, and (iv) MO with Rashba SOC. The additional model parameter values are chosen as $\mu = 4.0\Delta_0$ and $t = \Delta_0$.

In Fig. S9(a) and (b), we depict the eigenvalue spectrum in the topological phase for SO and MO cases [at the level of tight-binding model Eq. (4) of our main text], respectively. The strength of the Rashba SOC in both

cases has been varied to illustrate its impact on our results. The qualitative similarity of the overall physics in the presence of moderate strength Rashba SOC is evident from the results presented in Fig. S9(a) for the SO model. However, for strong Rashba SOC strength ($\lambda_R = 0.7\Delta$), the MFEM becomes relatively dispersive without altering the topological nature of the TSC phase. Incorporating additional orbital channels in the MO model and including the SOC term (Eq. S16) does not alter the existence of MFEMs in the topological phase. We observe only slight overall renormalization in the gapless topological superconducting phase hosting nondispersive MFEMs. Indeed, the fundamental physics of MFEMs remains qualitatively similar even with the inclusion of various basic ingredients such as multi-orbital channels and the Rashba SOC term. In Fig. S9(c), we demonstrate the bulk gap (ΔG) profile as a function of exchange coupling strength J for four different scenarios: (i) SO without Rashba SOC, (ii) SO with Rashba SOC, (iii) MO without Rashba SOC, (iv) MO with Rashba SOC. Notably, the topological gapless phase is observed to exist approximately between $J = 3.5\Delta_0$ and $J = 4.7\Delta_0$ for all the scenarios mentioned above. Hence, the presence of additional orbital channels and the effect of SOC has minimal influence on the overall physics of MFEMs.

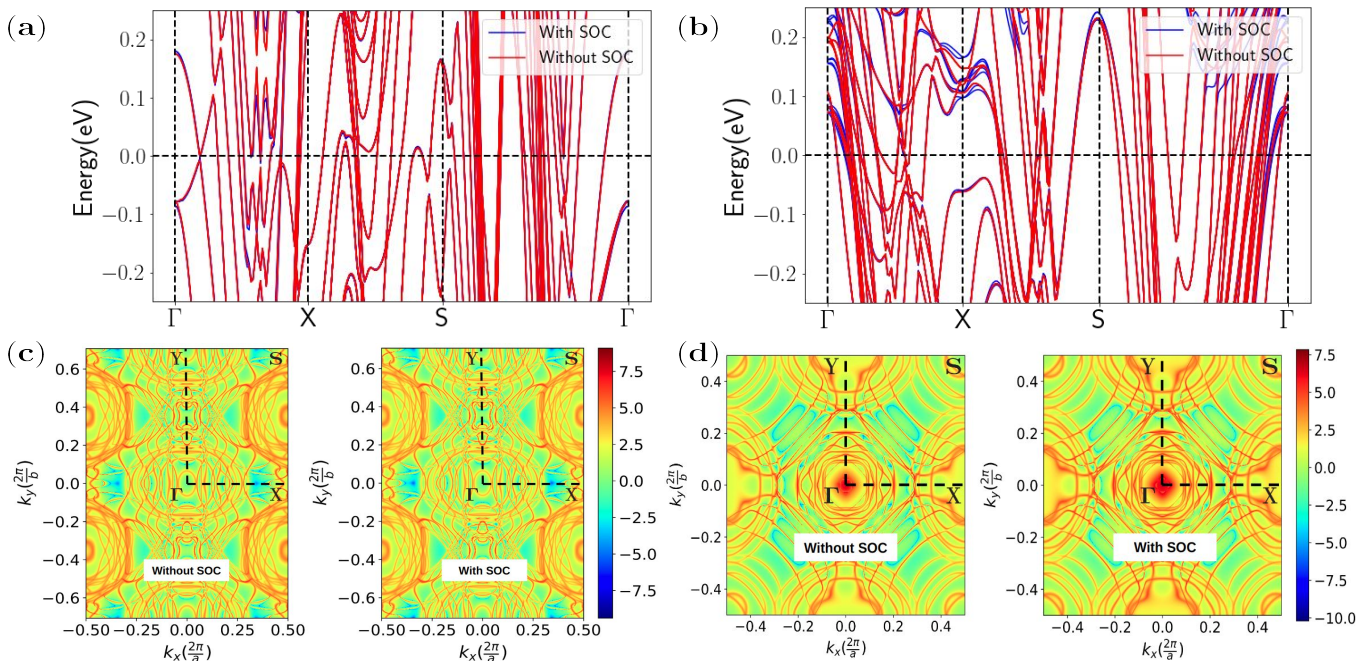


FIG. S10. The panels labelled as (a) and (b) display the band structures obtained from the *ab initio* electronic structure calculations for the Nb(110) and Nb(001) surfaces, respectively. These band structures are computed with and without taking into account the effect of SOC. Furthermore, the panels labelled as (c) and (d) display the energy contours of the Fermi surface for both surfaces. Similar to the band structure panels, these Fermi surface energy contours are also computed with and without considering SOC.

In the main text, we opted for the minimal model without including the SOC term to provide a clear and unambiguous exploration of the real example systems. The choice was based on the empirical observation that the real example systems we studied are not significantly influenced by the Rashba SOC term, which may observe in surface/interface systems. In Fig. S10, we have presented the band structure and the Fermi surface plots for *s*-wave superconductor, Nb(110) and Nb(001) in slab geometries. The influence of the SOC effect on the band structure is minimal, as evidenced by the negligible shifts in the blue and red bands in Fig. S10(a) and (b) for Nb(110) and Nb(001), respectively. Moreover, the Fermi surface plots for both cases, with and without SOC, shown in Fig. S10(c) and (d) for Nb surfaces, clearly demonstrate the minimal impact of the SOC effect.